https://doi.org/10.5194/egusphere-2026-3527
Preprint. Discussion started: 9 July 2026

Contrasting surface and column-averaged CO_2 responses over terrestrial China under carbon peaking and carbon neutrality emission pathways: anthropogenic, biospheric, and regional transport contributions

Kaiqiang Gu, Yi Yang*, Shixiang Su, Xiaoming Hu, Feifan Bian

Laboratory of Climate Resource Development and Disaster Prevention in Gansu Province, Center for Weather Forecasting and Climate Prediction of Lanzhou University, College of Atmospheric Sciences, Lanzhou University, Lanzhou 730000, China;

*** Correspondence:** Yi Yang, E-mail: yangyi@lzu.edu.cn

Abstract

Understanding how changes in anthropogenic carbon dioxide (CO_2) emissions affect surface CO_2 mole fraction (surface CO_2), column-averaged dry-air CO_2 mole fraction (XCO_2), and the relative contributions of anthropogenic emissions and biospheric fluxes is essential for evaluating the atmospheric effects of emission mitigation. In this study, the Weather Research and Forecasting Model coupled with the Vegetation Photosynthesis and Respiration Model (WRF-VPRM) was used to simulate three emission scenarios: a 2016 baseline, a 2030 carbon peaking scenario, and a 2060 carbon neutrality scenario, under identical meteorological fields constrained by observations. Contribution decomposition, sensitivity experiments, backward trajectory analysis, and potential source contribution function (PSCF) analysis were combined to

https://doi.org/10.5194/egusphere-2026-3527
Preprint. Discussion started: 9 July 2026

diagnose the response mechanisms of atmospheric CO_2. Anthropogenic emissions increased by 18.1% in 2030 relative to 2016, whereas surface CO_2 and XCO_2 increased by only 0.363 and 0.065 ppm, respectively. In 2060, emissions decreased by 90.3%, reducing surface CO_2 and XCO_2 by 1.914 and 0.359 ppm, respectively. The XCO_2 response was therefore much weaker than the surface CO_2 response. Anthropogenic contributions dominated the differences among scenarios, while biospheric fluxes shaped seasonal variations and became relatively more important under deep emission reductions. The selected high-CO_2 episodes in the Beijing-Tianjin-Hebei (BTH) region were strongly modulated by meteorological conditions. Local accumulation dominated under stagnant conditions, whereas upstream transport dominated under favorable transport conditions. These results indicate that atmospheric CO_2 responses to carbon peaking and carbon neutrality pathways are jointly shaped by anthropogenic mitigation, biospheric fluxes, and regional transport.

Keywords: carbon neutrality; carbon peaking; WRF-VPRM; atmospheric CO_2; XCO_2; anthropogenic emissions; regional transport

1. Introduction

The goals of carbon peaking and carbon neutrality are reshaping China's anthropogenic CO_2 emissions, with expected changes in total emissions, sectoral composition, and spatial distribution (IEA, 2021;

https://doi.org/10.5194/egusphere-2026-3527
Preprint. Discussion started: 9 July 2026

Zhang and Chen, 2022a, b). Previous studies have developed future emission pathways for China and evaluated their implications for energy transition, coordinated air pollution control, health benefits, and regional mitigation potential (Tong et al., 2020; Cheng et al., 2023; Zhang et al., 2024; Zhong et al., 2025). These studies provide an important basis for understanding emission mitigation pathways, but how pathway changes are translated into atmospheric CO2 mole-fraction responses remains insufficiently quantified. Changes in anthropogenic emissions do not translate proportionally into atmospheric CO_2 mole fractions, because atmospheric CO_2 also reflects biospheric exchange and atmospheric transport (Ciais et al., 2013; Le Quéré et al., 2018; Canadell et al., 2021; Friedlingstein et al., 2025). This complexity becomes more evident when CO_2 is examined at different vertical scales. Surface CO_2 is closely linked to local emissions and boundary-layer processes, whereas column-averaged dry-air CO_2 mole fraction (XCO_2), as observed by satellite missions such as the Orbiting Carbon Observatory-2 (OCO-2), represents a vertically integrated signal (Crisp et al., 2004; O'Dell et al., 2012; Eldering et al., 2017; Wunch et al., 2017). Recent studies have used satellite observations and regional model simulations to detect urban CO_2 plumes, analyze spatiotemporal variability, and estimate anthropogenic emissions in key regions (Zheng et al., 2020; Chen et al., 2024; Sheng et al., 2025). However, satellite observations alone cannot fully separate the

https://doi.org/10.5194/egusphere-2026-3527
Preprint. Discussion started: 9 July 2026

effects of anthropogenic emissions, biospheric fluxes, and atmospheric transport. High-resolution regional models have therefore been widely used to simulate urban and regional CO_2 variability and to assess the roles of emissions and transport (Pillai et al., 2012; Feng et al., 2016; Li et al., 2020; Dong et al., 2021). Previous applications of the Weather Research and Forecasting model coupled with the Vegetation Photosynthesis and Respiration Model (WRF-VPRM) have mainly focused on historical CO_2 variability, regional budgets, and urban-scale emission signals (Park et al., 2018; Hu et al., 2020). Among these models, WRF-VPRM couples mesoscale meteorology with biospheric CO_2 exchange estimated from satellite-derived vegetation indices and meteorological variables, allowing anthropogenic emissions, biospheric fluxes, and atmospheric transport to be represented within a consistent three-dimensional framework (Ahmadov et al., 2007, 2009; Mahadevan et al., 2008). Despite these advances, it remains unclear how China's carbon peaking and carbon neutrality emission pathways affect surface CO_2 and XCO_2 differently, and how anthropogenic and biospheric contributions change from the peaking stage to deep emission reductions.

Regional CO_2 concentrations are also strongly modulated by meteorological processes. Weather systems, frontal processes, wind field variations, and atmospheric boundary-layer height can alter CO_2 accumulation, dilution, and horizontal transport, leading to rapid changes

https://doi.org/10.5194/egusphere-2026-3527
Preprint. Discussion started: 9 July 2026

in surface CO_2 (Chan et al., 2004; Hurwitz et al., 2004; Parazoo et al., 2011; Díaz-Isaac et al., 2014, 2018; Hu et al., 2021). In eastern China, high-emission regions such as the Beijing-Tianjin-Hebei (BTH) region, Shandong, and the Yangtze River Delta contain dense urban and industrial CO2 emission sources (Cai et al., 2018; Dong et al., 2021). Previous satellite and regional modeling studies have shown that CO2 signals over these regions are affected by both local emissions and regional transport (Zheng et al., 2020; Dong et al., 2021; Sheng et al., 2025). Under future mitigation pathways, changes in total emissions and spatial emission patterns may alter the relative importance of local and transported CO_2 contributions. This issue remains insufficiently quantified for key high-emission regions.

To address these gaps, this study used the online coupled WRF-VPRM model to simulate atmospheric CO_2 over terrestrial China under three anthropogenic emission scenarios: a 2016 baseline scenario, a 2030 carbon peaking scenario, and a 2060 carbon neutrality scenario. All simulations were driven by identical meteorological fields to isolate the atmospheric CO_2 responses to emission pathway changes. Specifically, we examined three aspects. First, we compared the magnitude, spatial distribution, and seasonal variation of surface CO_2 and XCO_2 among the three emission scenarios. Second, we quantified the contributions of anthropogenic emissions and biospheric fluxes to CO_2 variations as

https://doi.org/10.5194/egusphere-2026-3527
Preprint. Discussion started: 9 July 2026

emissions changed from the carbon peaking scenario toward carbon neutrality. Third, we analyzed how local accumulation and regional transport shaped high-CO_2 episodes in the Beijing-Tianjin-Hebei (BTH) region. By combining component decomposition, sensitivity experiments, backward trajectory analysis, and potential source contribution function (PSCF) analysis, this study quantifies the contrasting responses of surface CO_2 and XCO_2 and clarifies the roles of anthropogenic mitigation, biospheric fluxes, and regional transport.

2. Data and Methods

2.1 Model configuration

To quantify the response of atmospheric CO_2 concentrations over terrestrial China to different emission pathways, this study used the online coupled WRF-VPRM system. The system simulates meteorological evolution, atmospheric transport, biospheric CO_2 exchange, and atmospheric CO_2 concentrations within the same dynamical framework. It also transports CO_2 from different sources as independent tagged passive tracers (Ahmadov et al., 2007). This tracer design allows the contributions of background CO_2, biospheric fluxes, and anthropogenic emissions to the total CO_2 concentration to be quantified. Net ecosystem CO_2 exchange was calculated online by VPRM. VPRM estimates gross primary production and ecosystem respiration from satellite-derived enhanced vegetation index and land surface water

https://doi.org/10.5194/egusphere-2026-3527
Preprint. Discussion started: 9 July 2026

index, together with meteorological variables such as temperature, shortwave radiation, and photosynthetically active radiation. It then provides hourly net ecosystem exchange (Mahadevan et al., 2008).

To isolate the effects of emission pathway changes, all scenario simulations were conducted under identical meteorological initial and boundary conditions and forcing. The meteorological fields were constrained using four-dimensional data assimilation (FDDA) nudging (Stauffer and Seaman, 1990, 1994). Specifically, observational nudging was applied below the planetary boundary layer to assimilate near-surface air temperature observations from the NCEP ADP (National Centers for Environmental Prediction Automated Data Processing) dataset (National Centers for Environmental Prediction et al., 2008), while grid nudging was applied above the planetary boundary layer using ERA5 (ECMWF Reanalysis v5) reanalysis fields. This configuration kept the meteorological fields consistent among the three emission scenarios and reduced the influence of meteorological variability on the simulated CO_2 differences.

The model domain covered China and its surrounding areas to reduce the influence of lateral boundary inputs on the results over China. The domain was centered at 36.461°N, 102.531°E, with a horizontal resolution of 12 km, 416 × 355 grid cells, 50 vertical layers, and a model top of 50 hPa. The model was restarted monthly. For each monthly

https://doi.org/10.5194/egusphere-2026-3527
Preprint. Discussion started: 9 July 2026

simulation, the last 10 d of the preceding month was used as spin-up and was excluded from the statistical analysis. Figure 1 shows the model domain, the key study region, the meteorological observation sites used for observational nudging, and the backward trajectory receptor point.

The initial and boundary meteorological fields were derived from ERA5 data, with a spatial resolution of 0.25° × 0.25° and a temporal resolution of 6 h (Hersbach et al., 2020). The initial and boundary conditions for CO_2 were obtained from the CAMS (Copernicus Atmosphere Monitoring Service) global inversion-optimised greenhouse gas fluxes and concentrations dataset, with a spatial resolution of 1° × 1° and a temporal resolution of 6 h (Copernicus Atmosphere Monitoring Service, 2020). The main physical parameterizations included the Lin microphysics scheme (Chen and Sun, 2002), the CAM longwave and shortwave radiation schemes (Neale et al., 2010), the YSU planetary boundary-layer scheme (Hong et al., 2006), the Noah land surface scheme (Tewari et al., 2004), and the new Grell cumulus convection scheme (Grell, 1993; Grell and Dévényi, 2002).

To isolate the influence of anthropogenic emission pathways, the 2016, 2030, and 2060 baseline simulations used identical meteorological forcing, nudging settings, physical parameterizations, CO_2 initial and boundary conditions, and biogenic flux calculation schemes. The 2016 vegetation indices and VPRM parameters were also fixed across all

https://doi.org/10.5194/egusphere-2026-3527
Preprint. Discussion started: 9 July 2026

simulations. This design allowed differences in CO_2 among scenarios to be attributed mainly to changes in anthropogenic emission inputs. It therefore provided a clear basis for quantifying the surface CO_2 and XCO_2 responses induced by changes in emission pathways.

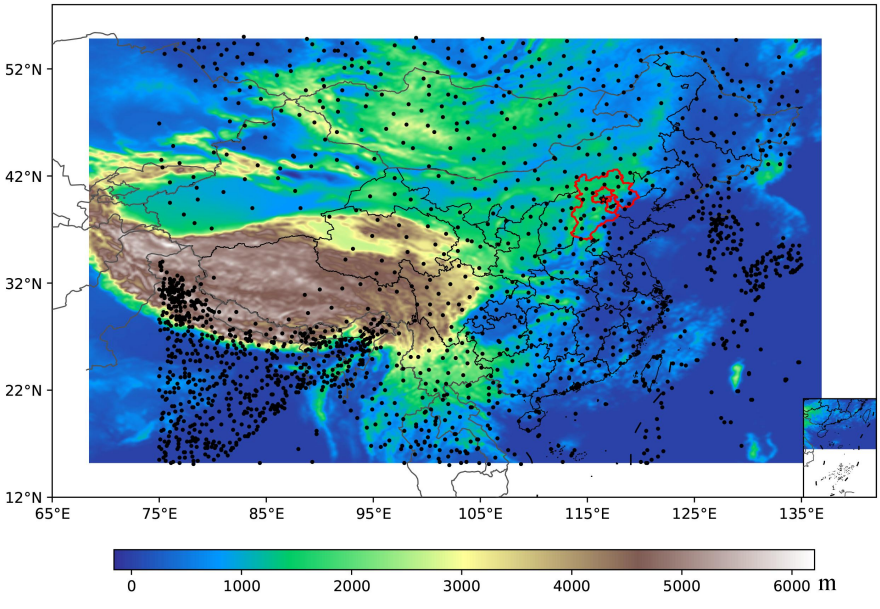

Figure 1. Model domain and observational sites used for observational nudging. Shading indicates terrain height (m), black dots indicate meteorological observation sites, the star marks the receptor point for backward trajectory analysis (39.8°N, 116.5°E), and the red provincial boundaries indicate the BTH region where anthropogenic CO_2 emissions were set to zero in the sensitivity experiments.

2.2 Emission scenarios

Three anthropogenic CO_2 emission experiments were designed: a 2016 baseline scenario, a 2030 carbon peaking scenario, and a 2060

https://doi.org/10.5194/egusphere-2026-3527
Preprint. Discussion started: 9 July 2026

carbon neutrality scenario. The 2016 scenario represents the spatial pattern and sectoral structure of China's anthropogenic CO_2 emissions under the historical baseline. The 2016 emission data were obtained from the MEIC (Multi-resolution Emission Inventory for Climate and Air Pollution Research) V2.0 inventory, which includes the agricultural, industrial, power, residential, and transportation sectors (Xu et al., 2023; Geng et al., 2024). The 2030 and 2060 scenarios were based on the on-time peak net-zero clean-air pathway from Dynamic Projection model for Emissions in China (DPEC) V1.2 and represent the carbon peaking and carbon neutrality stages, respectively (Cheng et al., 2023; Tong et al., 2020). All emission data were processed consistently into the CO_2 emission inputs required by WRF-VPRM, including unit conversion, sectoral classification, spatial interpolation, temporal allocation, and model-grid matching. For the future scenarios, the changes in national total emissions, sectoral structure, and spatial distribution provided by DPEC V1.2 were retained. The same input-processing procedure used for the 2016 baseline scenario was applied to reduce the influence of emission preprocessing on the scenario comparison.

Additional sensitivity experiments were conducted to distinguish the contributions of local anthropogenic emissions from the BTH region and external regional transport to CO_2 concentrations. The baseline experiments retained anthropogenic emissions over the entire model

https://doi.org/10.5194/egusphere-2026-3527
Preprint. Discussion started: 9 July 2026

domain. The sensitivity experiments turned off only anthropogenic emissions from the BTH region. Emissions from other regions, meteorological fields, biogenic fluxes, and boundary conditions were identical to those in the corresponding baseline experiments. The experimental design is summarized in Table 1.

Table 1. Design of the baseline and sensitivity experiments.

Experiment name	Emission scenario design
BASE_2016	Anthropogenic CO_2 emissions from MEIC V2.0 for 2016 were used as the baseline emission scenario.
SEN_noBTH_2016	Anthropogenic CO_2 emissions in the BTH region were set to zero, while emissions from other regions were kept the same as in BASE_2016.
BASE_2030	Anthropogenic CO_2 emissions in 2030 under the on-time peak net-zero clean-air pathway from DPEC V1.2 were used as the carbon peaking emission scenario.
SEN_noBTH_2030	Anthropogenic CO_2 emissions in the BTH region were set to zero, while emissions from other regions were kept the same as in BASE_2030.
BASE_2060	Anthropogenic CO_2 emissions in 2060 under the on-time peak net-zero clean-air pathway from DPEC V1.2 were used as the carbon neutrality emission scenario.
SEN_noBTH_2060	Anthropogenic CO_2 emissions in the BTH region were set to zero, while emissions from other regions were kept the same as in BASE_2060.

2.3 Diagnostic variables

Two CO_2 concentration diagnostics were analyzed. The first was the near-surface atmospheric CO_2 concentration, defined as the CO_2 mole fraction at the lowest model level. This variable represents the combined effects of near-surface anthropogenic emissions, terrestrial ecosystem

https://doi.org/10.5194/egusphere-2026-3527
Preprint. Discussion started: 9 July 2026

exchange, boundary-layer mixing, and local transport, and is referred to here as surface CO_2. The second was the column-averaged dry-air CO_2 mole fraction, referred to as XCO_2. It was calculated by pressure-weighted integration of CO_2 concentrations across the model vertical layers and was used to characterize the column-averaged CO_2 response over the atmospheric column.

XCO_2 was calculated as follows:

$$XCO_2=\frac{\sum_{k=1}^{50}(CO_2\times\Delta p)_k}{p_{bottom}-p_{top}} \quad (1)$$

where CO_{2_k} is the CO_2 mole fraction in the kth vertical layer, Δp_k is the pressure thickness of that layer, k is the number of model vertical layers included in the integration, and p_{bottom} and p_{top} denote the pressure at the bottom and top of the model vertical column, respectively. In this study, XCO_2 was calculated using the layer-by-layer pressure thickness from the WRF-VPRM output and was used for model validation and analysis of the emission pathway responses.

To quantify the contributions of different sources to atmospheric CO_2 concentrations, the model output included three CO_2 tracer components: the background component, the biogenic component, and the anthropogenic component. Total CO_2 can be expressed as follows:

$$CO_2^{Total}=CO_2^{ANT}+CO_2^{BIO}+CO_2^{BCK} \quad (2)$$

Correspondingly, XCO_2 can be expressed as follows:

https://doi.org/10.5194/egusphere-2026-3527
Preprint. Discussion started: 9 July 2026

$$XCO_2^{Total}=XCO_2^{ANT}+XCO_2^{BIO}+XCO_2^{BCK} \quad (3)$$

where CO_2^{ANT} represents the concentration enhancement caused by anthropogenic emissions, CO_2^{BIO} represents the concentration change caused by net terrestrial ecosystem CO_2 exchange, and CO_2^{BCK} represents the background CO_2 contribution determined by the initial and boundary conditions. The corresponding column concentration components are denoted as XCO_2^{ANT}, XCO_2^{BIO}, and XCO_2^{BCK}, respectively. In this study, a positive biogenic contribution indicates an increase in CO_2 concentration caused by net ecosystem release, while a negative value indicates a decrease in CO_2 concentration caused by net ecosystem uptake.

To quantify the attenuation of the surface CO_2 signal during its transfer to the full atmospheric column, an attenuation factor was defined as follows:

$$F_{att}=\frac{\Delta XCO_2}{\Delta surface\ CO_2} \quad (4)$$

where ΔXCO_2 and $\Delta surface\ CO_2$ represent the changes in XCO_2 and surface CO_2 in a future scenario relative to the 2016 baseline scenario, respectively. A smaller F_{att} indicates stronger dilution of the near-surface concentration signal during column averaging.

The seasonal amplitude of the anthropogenic contribution, the biogenic contribution, and their combined contribution was defined as the difference between the maximum and minimum values of the monthly

https://doi.org/10.5194/egusphere-2026-3527
Preprint. Discussion started: 9 July 2026

mean series within a year.

$$A=X_{max}-X_{min} \tag{5}$$

2.4 Validation data and evaluation metrics

The Mapping-XCO_2 dataset (Sheng et al., 2023) was used to evaluate the ability of the model to simulate atmospheric CO_2 over China in 2016. This dataset has a spatial resolution of 1° × 1° and a temporal resolution of 3 d. It integrates multi-source satellite XCO_2 observations and fills data gaps, providing a continuous reference for regional-scale spatiotemporal variations in XCO_2.

Model performance was evaluated using three metrics: the correlation coefficient (R), mean bias (MB), and root mean square error (RMSE). R measures the consistency of temporal variations between the simulations and observations. MB characterizes the systematic model bias, and RMSE represents the overall magnitude of the simulation error. These metrics were calculated as follows:

$$R=\frac{\sum_{i=1}^{n}(M_i-\overline{M})(O_i-\overline{O})}{\sqrt{\sum_{i=1}^{n}(M_i-\overline{M})^2}\sqrt{\sum_{i=1}^{n}(O_i-\overline{O})^2}} \tag{6}$$

$$MB=\frac{1}{n}\sum_{i=1}^{n}(M_i-O_i) \tag{7}$$

$$RMSE=\sqrt{=\frac{1}{n}\sum_{i=1}^{n}(M_i-O_i)^2} \tag{8}$$

In the equation, M_i and O_i denote the simulated and reference values for the ith sample, respectively; $\overline{M}$ and $\overline{O}$ denote the mean

https://doi.org/10.5194/egusphere-2026-3527
Preprint. Discussion started: 9 July 2026

simulated and reference values, respectively; and n is the number of samples. The 2016 validation results were used to evaluate the ability of the model to reproduce XCO_2 variations over China and to provide a basis for the reliability of the subsequent scenario analysis.

2.5 Contribution decomposition and regional transport analysis

For the contribution analysis, the BTH region was treated as the receptor region. Local emission and external regional transport contributions were separated using sensitivity experiments in which anthropogenic CO_2 emissions in the BTH region were set to zero. Let $CO_2^{ANT}{}_{BASE}$ denote the anthropogenic CO_2 contribution in the baseline experiment, and $CO_2^{ANT}{}_{SEN\_noBTH}$ denote the corresponding result after anthropogenic emissions in the BTH region were set to zero. For the BTH receptor region, the local emission contribution was defined as follows:

$$CO_2^{local\_BTH}=CO_2^{ANT}{}_{BASE}-CO_2^{ANT}{}_{SEN\_noBTH} \quad (9)$$

After emissions in the BTH region were set to zero, the remaining anthropogenic CO_2 in the BTH region mainly originated from emissions outside the region that were transported into the BTH region. The external transport contribution was therefore defined as follows:

$$CO_2^{transport\_toBTH}=CO_2^{ANT}{}_{SEN\_noBTH} \quad (10)$$

The fractions of the external transport contribution and the local contribution, together with the local-to-transport ratio, were calculated as follows:

https://doi.org/10.5194/egusphere-2026-3527
Preprint. Discussion started: 9 July 2026

$$R_{transport\_toBTH}=\frac{CO_2^{transport\_toBTH}}{CO_2^{ANT}{}_{BASE}}\times 100\% \quad (11)$$

$$R_{local\_BTH}=\frac{CO_2^{local\_BTH}}{CO_2^{ANT}{}_{BASE}}\times 100\% \quad (12)$$

$$f=\frac{CO_2^{local\_BTH}}{CO_2^{transport\_toBTH}} \quad (13)$$

By comparing $CO_2^{local\_BTH}$, $CO_2^{transport\_toBTH}$, and their corresponding fractions, the dominant control on anthropogenic CO_2 enhancement in the BTH region could be identified under different emission pathways.

In the regional case analysis, high-CO_2 episodes were identified using the hourly anthropogenic CO_2 contribution at the backward trajectory receptor point. They were then classified using the contribution decomposition and meteorological background. An episode was classified as locally dominated when the local emission contribution accounted for at least 70% of the anthropogenic CO_2 enhancement, exceeded the external transport contribution by at least 30 percentage points, and was accompanied by weak winds, a relatively low boundary layer, and regional stagnation. An episode was classified as transport dominated when the external transport contribution accounted for at least 70%, exceeded the local contribution by at least 30 percentage points, and occurred under favorable transport conditions. Based on these criteria, 14 to 16 January was selected as the locally dominated episode, and 26 to 28 January was selected as the transport-dominated episode.

https://doi.org/10.5194/egusphere-2026-3527
Preprint. Discussion started: 9 July 2026

Backward trajectory and PSCF analyses were conducted to identify upstream transport pathways and potential source regions (Ashbaugh et al., 1985; Zeng and Hopke, 1989; Stein et al., 2015; Rolph et al., 2017). Backward trajectories were calculated using the Hybrid Single-Particle Lagrangian Integrated Trajectory (HYSPLIT) model driven by the meteorological fields simulated by WRF-VPRM. The trajectory receptor point was located at 39.8°N, 116.5°E, with a starting height of 100 m and a backward tracking duration of 72 h.

PSCF was used to estimate the probability that potential source regions contributed to high-CO_2 episodes at the receptor point. The hourly external transport contribution $CO_2^{transport\_toBTH}$ was used as the criterion variable. This reduced the influence of background-field variations and local accumulation on the identification of potential source regions. PSCF was defined as follows:

$$PSCF_{ij}=\frac{m_{ij}}{n_{ij}} \tag{14}$$

where n_{ij} is the number of times that all backward trajectories passed through grid cell (i,j), and m_{ij} is the number of trajectory endpoints in that grid cell for which the corresponding external transport contribution at the receptor point exceeded the prescribed threshold. The threshold was defined as the 70th percentile of hourly $CO_2^{transport\_toBTH}$ during the corresponding case period. To reduce the instability caused by grid cells with a small number of trajectory endpoints, a weighting factor

https://doi.org/10.5194/egusphere-2026-3527
Preprint. Discussion started: 9 July 2026

W_{ij} was applied to correct PSCF:

$$WPSCF=W_{ij}\times PSCF_{ij} \quad (15)$$

where W_{ij} was determined according to the number of trajectory endpoints in each grid cell and was defined as follows:

$$W_{ij}=\begin{cases}1.00, & 80<n_{ij}\\ 0.70, & 20<n_{ij}\leq 80\\ 0.42, & 10<n_{ij}\leq 20\\ 0.05, & n_{ij}\leq 10\end{cases} \quad (16)$$

By combining sensitivity experiments, contribution decomposition, backward trajectory analysis, and PSCF analysis, this study explained the roles of local emissions and regional transport in high CO_2 episodes in the BTH region from the perspectives of both contribution magnitude and transport pathways.

3. Results

3.1 Evaluation of simulated XCO_2 over China

Before analyzing the responses to different emission pathways, the 2016 simulation of China-averaged XCO_2 was evaluated using the Mapping-XCO_2 dataset. As shown in Fig. 2a, both the simulation and the dataset showed a consistent seasonal cycle. XCO_2 increased in spring and reached its annual maximum from April to May, decreased in summer as terrestrial ecosystem uptake strengthened, reached its annual minimum from August to September, and then rebounded in autumn and winter. WRF-VPRM reproduced this seasonal phase reasonably well. The simulation showed a slight positive bias relative to Mapping-XCO_2, with

https://doi.org/10.5194/egusphere-2026-3527
Preprint. Discussion started: 9 July 2026

an MB of 0.776 ppm, an RMSE of 0.942 ppm, and an R of 0.986. The scatter density distribution in Fig. 2b further shows that most samples were clustered near the 1:1 line. The fitted line was slightly above the 1:1 line, consistent with the weak positive bias in the time series.

This evaluation indicates that WRF-VPRM reasonably reproduced the seasonal variation and concentration magnitude of XCO_2 over China in 2016. It supports the subsequent analysis of differences in the responses of surface CO_2 and XCO_2 over terrestrial China under different emission pathways.

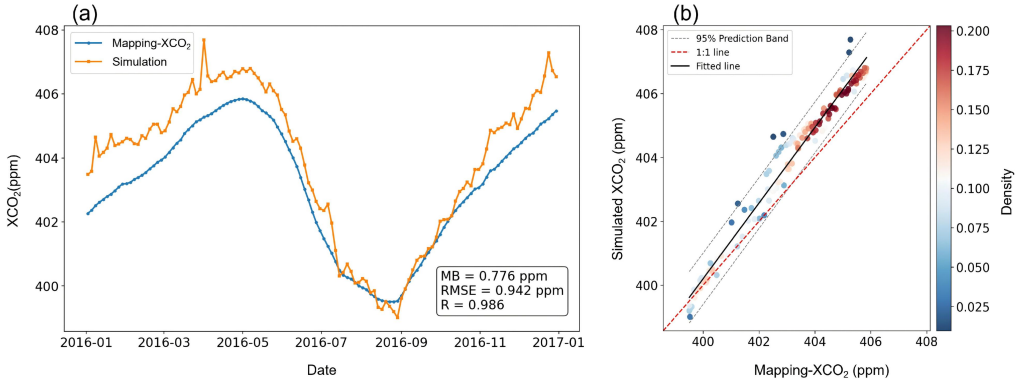

Figure 2. Comparison of simulated China-averaged XCO_2 in 2016 with the Mapping-XCO_2 dataset. (a) Time series of China-averaged XCO_2. (b) Scatter density plot of simulated XCO_2 against Mapping-XCO_2. The red dashed line indicates the 1:1 line, the black solid line indicates the linear fit, the gray dashed lines indicate the 95% prediction interval, and the colors indicate sample density.

3.2 Differences in anthropogenic CO_2 emissions among the three

https://doi.org/10.5194/egusphere-2026-3527
Preprint. Discussion started: 9 July 2026

pathways

Before analyzing atmospheric CO_2 responses, it is necessary to characterize the anthropogenic CO_2 emission inputs under the different pathways. As shown in Fig. 3a, national anthropogenic CO_2 emissions in 2016 were 9084.29 Mt yr^{-1}. The industrial and power sectors contributed 4741.26 and 2850.34 Mt yr^{-1}, respectively, together accounting for 83.6% of the national total. Under the 2030 carbon peaking scenario, national emissions increased to 10724.27 Mt yr^{-1}, about 18.1% higher than in 2016. The increase mainly came from the power and industrial sectors, with the power sector alone increasing by 1265.24 Mt yr^{-1}. Under the 2060 carbon neutrality scenario, national anthropogenic CO_2 emissions decreased to 876.80 Mt yr^{-1}, representing reductions of about 90.3% relative to 2016 and 91.8% relative to 2030. The remaining emissions were mainly concentrated in the industrial and transportation sectors, which contributed 598.70 and 186.52 Mt yr^{-1}, accounting for 68.3% and 21.3%, respectively. Emissions from the power sector decreased to 11.13 Mt yr^{-1}. These results indicate that deep emission reductions were mainly reflected in large decreases in power and industrial emissions, whereas residual emissions were concentrated in industrial and transportation sectors that are harder to eliminate completely. Figures 3b to d show the monthly emission variations. Emissions were higher in winter and lower in summer in both 2016 and 2030. Monthly emissions in 2030 were

https://doi.org/10.5194/egusphere-2026-3527
Preprint. Discussion started: 9 July 2026

396 generally higher than those in 2016, with a more pronounced increase in
397 winter. In 2060, monthly emissions were strongly reduced in all months,
398 although weak seasonal variations remained. This suggests that residual
399 emissions from the industrial, transportation, and residential sectors may
400 still contribute to seasonal CO_2 variability after deep emission reductions.

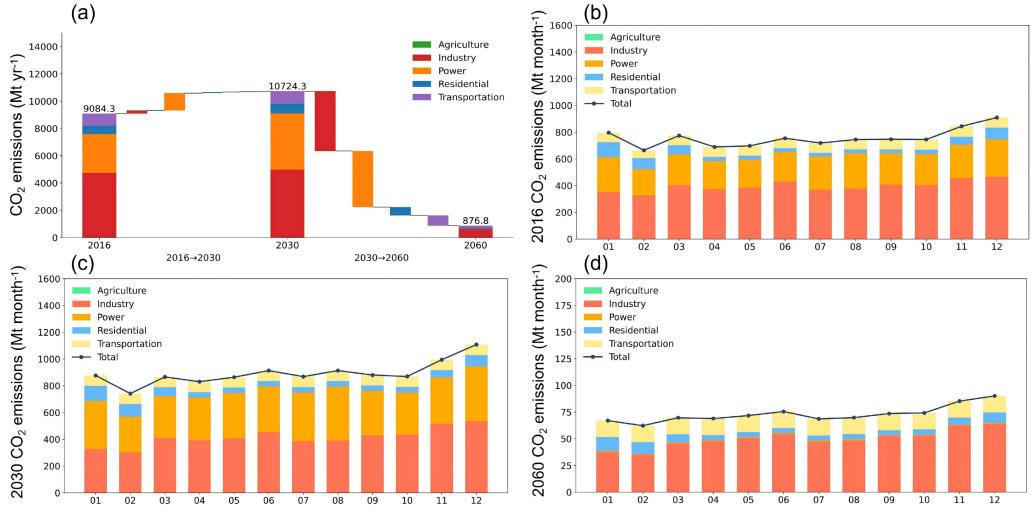

401

402 Figure 3. National total anthropogenic CO_2 emissions, sectoral
403 contributions, and monthly variations in 2016, 2030, and 2060. (a)
404 Annual total emissions and sectoral contribution decomposition (Mt yr^{-1}).
405 (b to d) Monthly anthropogenic CO_2 emissions and sectoral contributions
406 in 2016, 2030, and 2060, respectively (Mt $month^{-1}$).

407 Spatially, high anthropogenic CO_2 emissions in 2016 were
408 concentrated in urban agglomerations and industrial regions in eastern
409 and central China, including the BTH region, Shandong, the Yangtze
410 River Delta, the Pearl River Delta, Henan, Shanxi, and the

https://doi.org/10.5194/egusphere-2026-3527
Preprint. Discussion started: 9 July 2026

Chengdu-Chongqing region. In 2030, the spatial pattern of emissions largely followed the high-emission belts in 2016, with further enhancement in North China, East China, and some industrial cities in central and western China. In 2060, most high-emission regions across China were strongly weakened, and high-value areas contracted to a few industrial and urban agglomerations.

These results show that changes in emission pathways altered the national total emissions, sectoral structure, and spatial distribution. These changes further affected the magnitude, spatial pattern, and regional transport contribution of the surface CO_2 and XCO_2 responses.

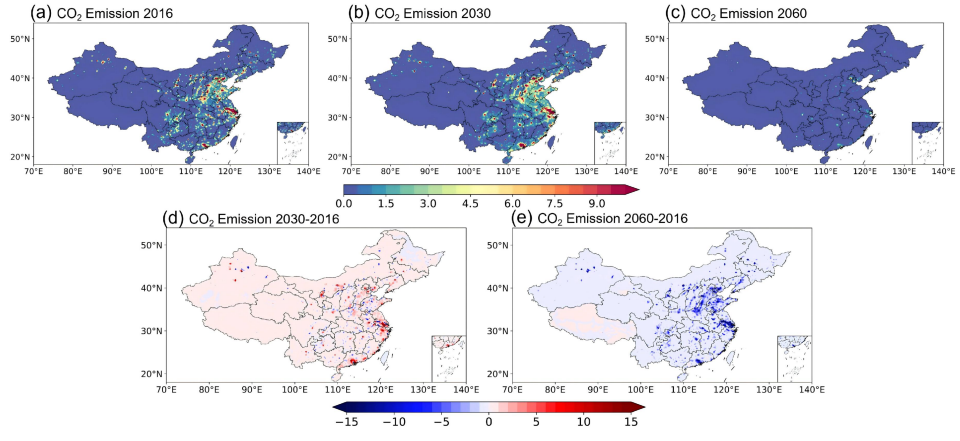

Figure 4. Spatial distributions and differences of anthropogenic CO_2 emissions over terrestrial China in 2016, 2030, and 2060. (a to c) Anthropogenic CO_2 emission intensities in 2016, 2030, and 2060, respectively. (d) Difference in emissions between 2030 and 2016. (e) Difference in emissions between 2060 and 2016. Positive values indicate

https://doi.org/10.5194/egusphere-2026-3527
Preprint. Discussion started: 9 July 2026

emission increases in the future scenarios, and negative values indicate emission reductions. Unit: Mt yr^{-1} $grid^{-1}$.

3.3 Responses of surface CO_2 and XCO_2 to different pathways

After characterizing the anthropogenic CO_2 emission inputs under the three pathways, we analyzed the responses of surface CO_2 and XCO_2 over terrestrial China. Figures 5a and b show that CO_2 concentrations increased only slightly in 2030 relative to 2016 and decreased markedly in 2060. The annual mean surface CO_2 increased from 407.40 ppm in 2016 to 407.76 ppm in 2030, an increase of 0.36 ppm. It then decreased to 405.49 ppm in 2060, 1.91 ppm lower than in 2016. XCO_2 showed the same direction of change but with a smaller magnitude, with values of 403.90, 403.97, and 403.54 ppm in 2016, 2030, and 2060, respectively. These results indicate that the emission increase during the carbon peaking stage produced a detectable but weak enhancement signal, while deep emission reductions under the carbon neutrality pathway substantially reduced CO_2 concentrations over China. The component contributions indicate that the background component largely set the absolute concentration levels of surface CO_2 and XCO_2. The anthropogenic contribution dominated the differences among scenarios, whereas the biogenic contribution mainly shaped the seasonal variations. Since the three scenarios used the same meteorological background, CO_2 initial conditions, and boundary conditions, the background component

https://doi.org/10.5194/egusphere-2026-3527
Preprint. Discussion started: 9 July 2026

varied little among scenarios. The anthropogenic contribution to surface CO_2 increased from 2.15 ppm in 2016 to 2.51 ppm in 2030 and decreased to 0.23 ppm in 2060. The anthropogenic contribution to XCO_2 increased from 0.40 to 0.47 ppm and then decreased to 0.04 ppm. This suggests that emission pathway changes affected total CO_2 mainly by changing the anthropogenic enhancement component. Figures 5c and d show that both surface CO_2 and XCO_2 were higher in winter and spring and lower in summer. For surface CO_2, the mean concentrations in winter and spring in 2016 were 411.62 and 411.16 ppm, respectively, while the summer mean decreased to 400.14 ppm. In 2030, concentrations were generally higher than those in 2016 in all seasons, with the winter mean increasing to 412.06 ppm. In 2060, concentrations decreased in all seasons, with the summer mean decreasing to 398.46 ppm. XCO_2 had the same seasonal phase as surface CO_2, but its daily variability and seasonal amplitude were smaller. These results indicate that enhanced terrestrial ecosystem uptake during the growing season can substantially offset the concentration enhancement caused by anthropogenic emissions. In the non-growing season, weaker biospheric uptake allows CO_2 concentrations to remain higher.

https://doi.org/10.5194/egusphere-2026-3527
Preprint. Discussion started: 9 July 2026

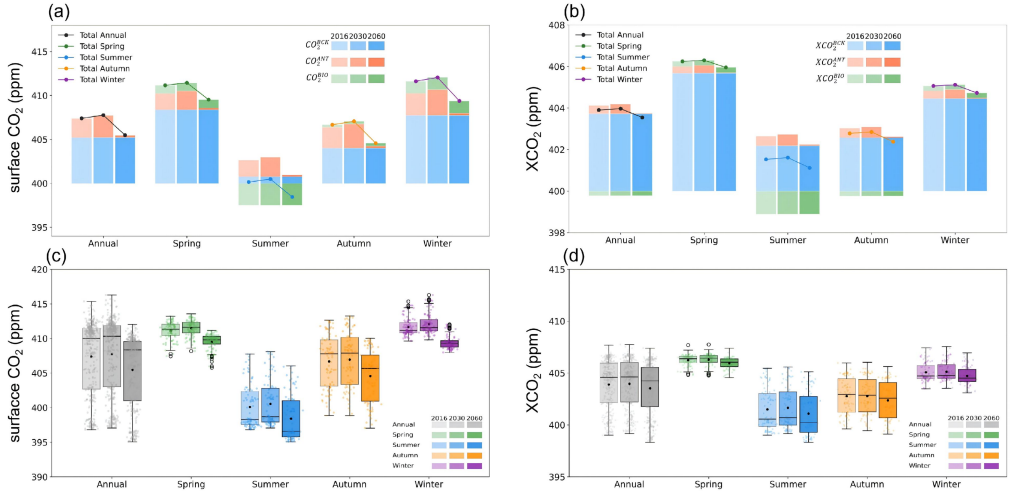

Figure 5. Annual mean, seasonal mean, and daily distributions of China-averaged surface CO_2 and XCO_2 in 2016, 2030, and 2060. (a) Annual and seasonal mean surface CO_2 concentrations and the contributions of the background, anthropogenic, and biogenic components under the three scenarios. (b) Annual and seasonal mean XCO_2 concentrations and the contributions of the background, anthropogenic, and biogenic components under the three scenarios. (c) Annual and seasonal boxplots of daily mean surface CO_2. (d) Annual and seasonal boxplots of daily mean XCO_2. Unit: ppm.

Spatially, high surface CO_2 values were mainly located in urban agglomerations and industrial activity centers in eastern and central China, including the BTH region, Shandong, the Yangtze River Delta, the Pearl River Delta, and central urban agglomerations. In 2030, the locations of high surface CO_2 values were generally consistent with those in 2016,

https://doi.org/10.5194/egusphere-2026-3527
Preprint. Discussion started: 9 July 2026

with slight enhancement over the original high-emission regions. In 2060, high-value centers in eastern and central China were markedly weakened, and spatial contrasts decreased as anthropogenic emissions were reduced. The XCO_2 spatial field was smoother. Its high-value areas extended from eastern high-emission regions to surrounding areas, and the scenario differences were weaker than those of surface CO_2. This indicates that surface CO_2 responds more directly to local emissions and boundary-layer accumulation, whereas XCO_2 reflects the combined effects of regional-scale accumulation, transport, and vertical averaging.

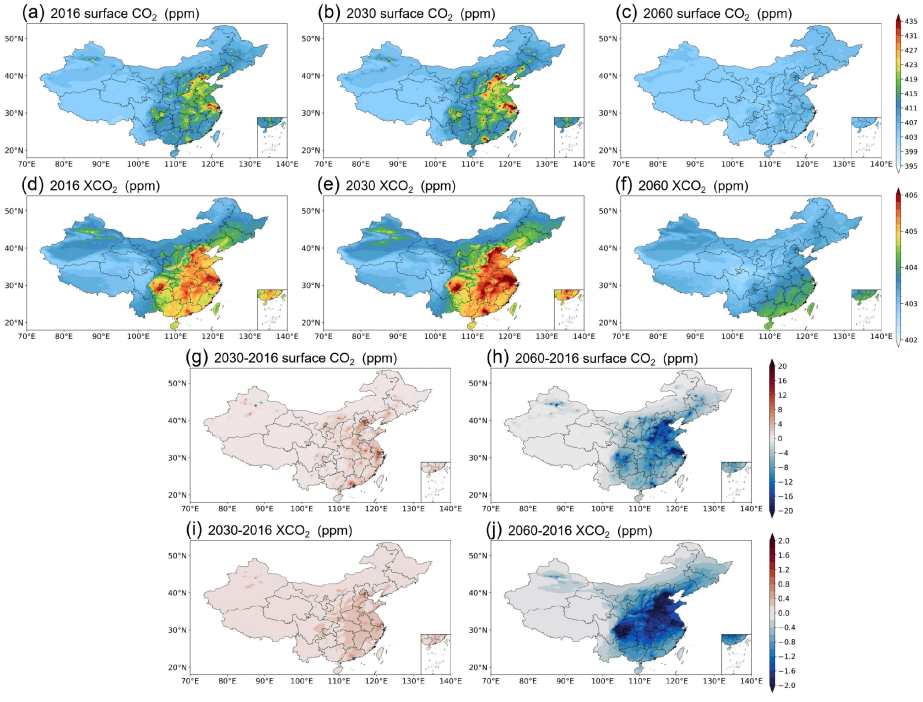

Figure 6. Spatial distributions and scenario differences of surface CO_2 and XCO_2 over terrestrial China in 2016, 2030, and 2060. (a to c) Annual mean spatial distributions of surface CO_2 in 2016, 2030, and 2060,

https://doi.org/10.5194/egusphere-2026-3527
Preprint. Discussion started: 9 July 2026

496 respectively. (d to f) Annual mean spatial distributions of XCO_2 in 2016,
497 2030, and 2060, respectively. (g) Difference in surface CO_2 between 2030
498 and 2016. (h) Difference in surface CO_2 between 2060 and 2016. (i)
499 Difference in XCO_2 between 2030 and 2016. (j) Difference in XCO_2
500 between 2060 and 2016. Positive values indicate higher CO_2
501 concentrations in the future scenarios, and negative values indicate lower
502 concentrations. Unit: ppm.

503 The vertical profiles in Fig. 7 further explain the difference in
504 response magnitude between surface CO_2 and XCO_2. Under all three
505 scenarios, CO_2 concentrations were higher in the lower layers and
506 gradually decreased with altitude, indicating that the anthropogenic
507 emission signal was mainly concentrated near the surface. In 2016 and
508 2030, lower-tropospheric CO_2 concentrations and vertical gradients were
509 relatively strong, and the lower-layer enhancement in 2030 was slightly
510 larger than that in 2016. In 2060, lower-layer CO_2 concentrations
511 decreased markedly and declined rapidly between 850 and 700 hPa.
512 Because XCO_2 is a pressure-weighted average over the atmospheric
513 column, the near-surface emission signal is diluted during column
514 averaging. Its scenario response is therefore much weaker than that of
515 surface CO_2. The attenuation factor F_{att} further quantified this
516 vertical-scale difference. On the annual mean scale, approximately 17.9%
517 to 18.8% of the surface CO_2 change relative to 2016 was reflected in

https://doi.org/10.5194/egusphere-2026-3527
Preprint. Discussion started: 9 July 2026

XCO_2 in 2030 and 2060. On the monthly scale, F_{att} ranged from 0.124 to 0.306 and from 0.142 to 0.294, respectively. This indicates that the vertical dilution effect was also influenced by seasonal boundary-layer structure and vertical mixing.

Overall, the CO_2 concentration response over terrestrial China showed a clear pathway dependence under the 2016, 2030, and 2060 emission pathways. The 2030 peaking pathway corresponded to a weak concentration enhancement, whereas the 2060 carbon neutrality pathway corresponded to a substantial concentration reduction. The background component provided the concentration baseline, the anthropogenic contribution determined the differences among scenarios, and the biogenic contribution shaped the seasonal phase. Surface CO_2 responded more directly to emission changes. XCO_2 retained the emission pathway signal, but this signal was strongly weakened by vertical integration and smoothing.

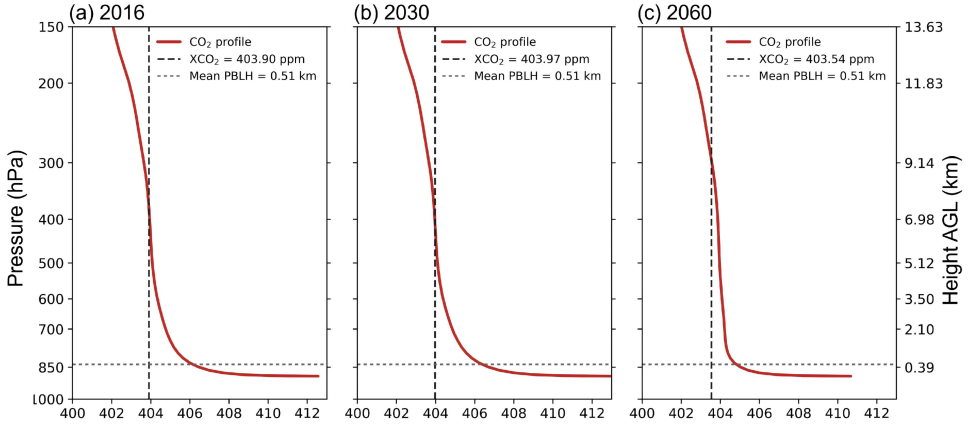

Figure 7. China-averaged vertical CO_2 profiles and the corresponding

https://doi.org/10.5194/egusphere-2026-3527
Preprint. Discussion started: 9 July 2026

XCO_2 in 2016, 2030, and 2060. (a to c) Vertical CO_2 profiles under the 2016, 2030, and 2060 scenarios, respectively. The red solid line indicates the variation in CO_2 concentration with pressure level, the black dashed line indicates the corresponding XCO_2, and the gray dashed line indicates the annual mean planetary boundary-layer height over terrestrial China. The left axis denotes pressure, and the right axis denotes height above ground level, with units of hPa and km, respectively. CO_2 and XCO_2 are both given in ppm.

Table 2. Attenuation factor for the response difference between surface CO_2 and XCO_2.

Scenario comparison	$\Delta surface\ CO_2$ (ppm)	ΔXCO_2 (ppm)	Annual F_{att}	Monthly F_{att} range
2030-2016	0.363	0.065	0.179	0.124 to 0.306
2060-2016	-1.914	-0.359	0.188	0.142 to 0.294

3.4 Contributions of anthropogenic and biogenic components to the CO_2 response

The previous section showed that CO_2 concentrations over terrestrial China increased weakly in 2030 and decreased substantially in 2060. To explain the sources of these pathway-dependent responses, we decomposed the CO_2 concentration changes beyond the background component into anthropogenic and biogenic contributions and analyzed their combined effects on the monthly scale. In Fig. 8, the anthropogenic

https://doi.org/10.5194/egusphere-2026-3527
Preprint. Discussion started: 9 July 2026

contribution represents the concentration enhancement caused by emissions, while the biogenic contribution represents the concentration change caused by net terrestrial ecosystem CO_2 exchange. Their sum represents the net concentration effect of the combined anthropogenic and biogenic contributions.

For surface CO_2, the anthropogenic contribution was positive throughout the year and acted as the direct source of concentration enhancement under all three pathways. In 2016 and 2030, the anthropogenic contribution was relatively strong, keeping the net effect positive in winter and spring. As emissions reached their peak in 2030, the anthropogenic contribution increased further. The combined anthropogenic and biogenic contribution reached 5.17 ppm in December, higher than the 4.45 ppm in 2016. The biogenic contribution showed a strong seasonal cycle. It became negative in summer when vegetation uptake strengthened and offset the anthropogenic enhancement from July to August. The combined contributions in July and August were -1.20 and -0.98 ppm in 2016 and narrowed to -0.90 and -0.58 ppm in 2030, respectively. This indicates that increased anthropogenic emissions during the carbon peaking stage weakened the near-surface CO_2 reduction caused by growing-season carbon uptake. In 2060, the contribution structure changed markedly. The anthropogenic contribution decreased substantially under deep emission reductions and was no longer sufficient

https://doi.org/10.5194/egusphere-2026-3527
Preprint. Discussion started: 9 July 2026

to offset biogenic uptake from June to September. The combined contribution therefore remained negative, reaching -2.73 and -2.90 ppm in July and August, respectively. The amplitude results further support this interpretation. The biogenic amplitude of surface CO_2 was 4.70 ppm under all three scenarios, indicating that the absolute seasonal variability of the biogenic contribution remained nearly unchanged under the experimental design with fixed vegetation indices, meteorological fields, and VPRM parameters. In contrast, the anthropogenic amplitude increased from 1.54 ppm in 2016 to 1.92 ppm in 2030 and then decreased to 0.17 ppm in 2060. In 2060, the amplitude of the combined contribution was 4.71 ppm, almost identical to the biogenic amplitude. This indicates that the seasonal variation in surface CO_2 under the carbon neutrality pathway was controlled more strongly by terrestrial ecosystem uptake and release.

XCO_2 retained a seasonal phase similar to that of surface CO_2, but both anthropogenic and biogenic signals were weakened by column averaging. In 2016 and 2030, the combined XCO_2 contribution was positive in winter and spring and became negative in summer. The positive contribution in March 2030 was 0.82 ppm, slightly higher than the 0.78 ppm in 2016. This indicates that the enhanced anthropogenic contribution under the carbon peaking pathway could still be transmitted to the column concentration. By 2060, the anthropogenic contribution

https://doi.org/10.5194/egusphere-2026-3527
Preprint. Discussion started: 9 July 2026

decreased markedly, and the relative role of the summer biogenic carbon sink increased. The combined XCO_2 contribution decreased to -1.60 ppm in August. Compared with surface CO_2, XCO_2 showed smaller monthly variability, indicating that near-surface signals were strongly smoothed during full-column integration. The amplitude analysis further shows that the seasonal variability of the anthropogenic contribution in XCO_2 was weak. The anthropogenic amplitudes of XCO_2 in 2016, 2030, and 2060 were 0.35, 0.45, and 0.04 ppm, respectively, much smaller than the corresponding biogenic amplitude of 2.06 ppm. By 2060, the anthropogenic amplitude became very small, while the amplitude of the combined contribution was 2.03 ppm, close to the biogenic amplitude. This indicates that, on the column-averaged scale, the biogenic contribution not only formed the summer minimum but also dominated the seasonal phase of XCO_2 under the deep-mitigation scenario.

Overall, the anthropogenic contribution determined the main concentration differences among the emission pathways, while the biogenic contribution mainly shaped the seasonal phase. As the anthropogenic contribution and its seasonal amplitude decreased substantially in 2060, the relative role of terrestrial ecosystem exchange in regulating CO_2 seasonality increased markedly. Because the anthropogenic contribution was the main source of CO_2 response differences among the pathways, the following regional case analysis

https://doi.org/10.5194/egusphere-2026-3527
Preprint. Discussion started: 9 July 2026

focuses on the local emission and external transport components within the anthropogenic contribution.

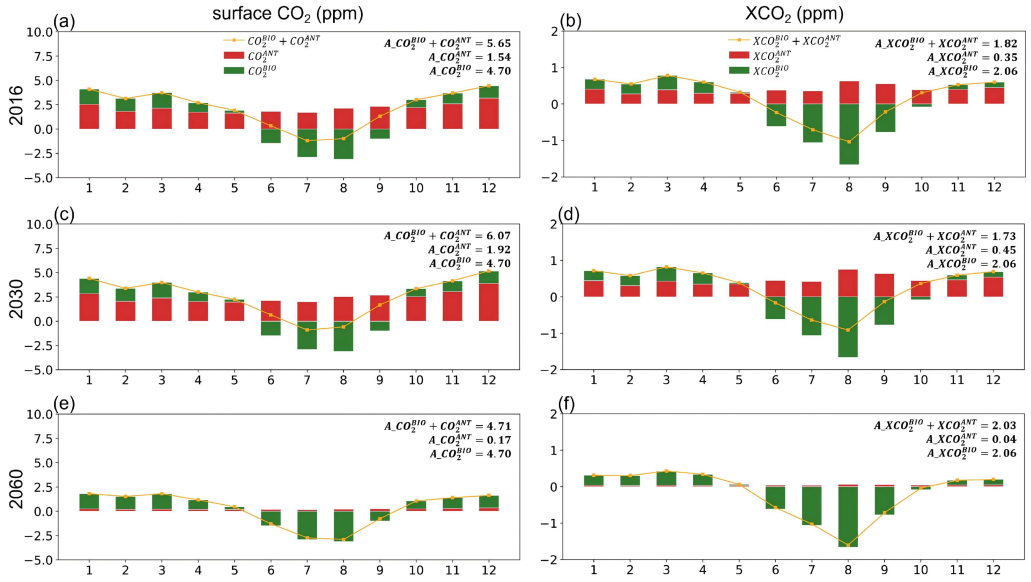

Figure 8. Monthly variations in the anthropogenic contribution, biogenic contribution, and their combined contribution to surface CO_2 and XCO_2 in 2016, 2030, and 2060. Red bars indicate the anthropogenic contribution, green bars indicate the biogenic contribution, and the yellow line indicates their combined contribution. Unit: ppm. *A* denotes the seasonal amplitude, defined as the difference between the maximum and minimum values of the 12-month mean series.

3.5 Regional case studies: local emissions versus regional transport

The anthropogenic contribution was the main source of CO_2 response differences among the emission pathways. This section therefore focuses on the internal structure of the anthropogenic contribution and

https://doi.org/10.5194/egusphere-2026-3527
Preprint. Discussion started: 9 July 2026

examines the relative roles of local emissions and external regional transport during high-CO_2 episodes in the BTH region. Two typical episodes were selected: 14 to 16 January, representing a locally dominated episode, and 26 to 28 January, representing a transport-dominated episode. The same contribution decomposition framework was applied to both cases. Anthropogenic CO_2 in the baseline and sensitivity experiments was decomposed into the local emission contribution from the BTH region and the external regional transport contribution. Backward trajectory and PSCF analyses were then used to identify the main transport pathways and potential source regions. PSCF was mainly used to identify potential source regions and transport pathways, while scenario differences in contribution intensity were evaluated using the quantitative results of the sensitivity experiments.

3.5.1 Locally dominated episode

During the 14 to 16 January episode, anthropogenic CO_2 concentrations in the BTH region were mainly controlled by local emission accumulation. As shown in Fig. 9, high anthropogenic CO_2 values in the 2016 and 2030 baseline experiments were concentrated over the BTH region and neighboring industrial and urban agglomerations. After anthropogenic emissions in the BTH region were set to zero, high values in the receptor region were markedly weakened. The near-surface wind fields in Fig. 9b, e, and h were weak. Airflow over the BTH region

https://doi.org/10.5194/egusphere-2026-3527
Preprint. Discussion started: 9 July 2026

and its surrounding areas showed slow transport and local stagnation, which favored the near-surface accumulation of local emissions. The corresponding local emission contribution formed clear near-source enhancement centers over Beijing, Tianjin, and central and southern Hebei. Table 3 further shows that the local contribution in the BTH region was 13.92 ppm in 2016, while the external transport contribution was 5.45 ppm. The local contribution accounted for 71.86%. In 2030, the local contribution increased to 21.34 ppm, and its fraction rose to 75.67%. In 2060, both the local and external transport contributions decreased substantially, while the fraction of the local contribution further increased to 86.90%. These results indicate that anthropogenic CO_2 concentrations during this episode were mainly controlled by local emissions in the BTH region. The emission increase in 2030 amplified local accumulation, whereas deep emission reductions in 2060 substantially weakened the absolute enhancement.

The backward trajectory and PSCF results indicate that the potential source regions of the locally dominated episode were relatively concentrated. The trajectories in Fig. 10 were mainly distributed over the western and eastern areas adjacent to the BTH region. The PSCF high-value regions showed a narrow-band distribution, mainly extending along the short-range transport corridor east of the BTH region. The PSCF spatial pattern was similar among the three scenarios, indicating

https://doi.org/10.5194/egusphere-2026-3527
Preprint. Discussion started: 9 July 2026

that under the same meteorological background, potential transport pathways were mainly determined by the airflow trajectories. In 2030, relatively high PSCF values were found near Shenyang, suggesting that this area was a comparatively strong potential source region. This result indicates that, under enhanced emissions in surrounding regions, high external transport events were more likely to occur along the transport pathway. Although a similar potential transport corridor remained in 2060, the external transport contribution in Table 3 decreased markedly, showing that deep emission reductions weakened the actual transport intensity along this pathway.

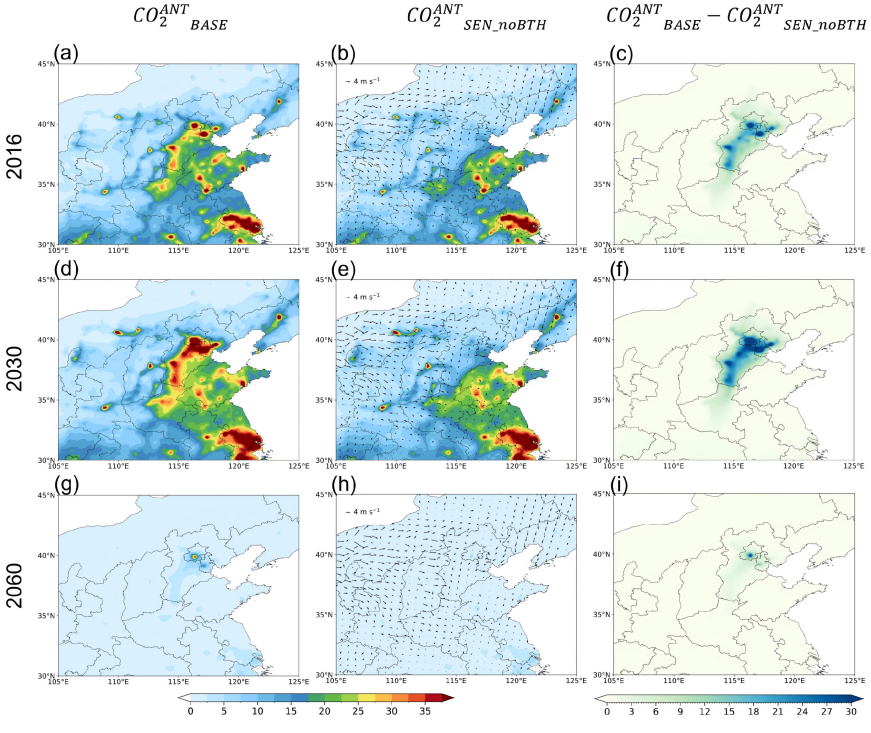

Figure 9. Decomposition of anthropogenic CO_2 contributions over the

https://doi.org/10.5194/egusphere-2026-3527
Preprint. Discussion started: 9 July 2026

Beijing-Tianjin-Hebei (BTH) region and surrounding areas during the locally dominated episode. (a, d, g) Anthropogenic CO_2 contributions in the baseline experiments for 2016, 2030, and 2060, respectively. (b, e, h) External regional transport contributions under the corresponding scenarios, with vectors indicating the near-surface wind field. (c, f, i) Local emission contributions from the BTH region. Unit: ppm.

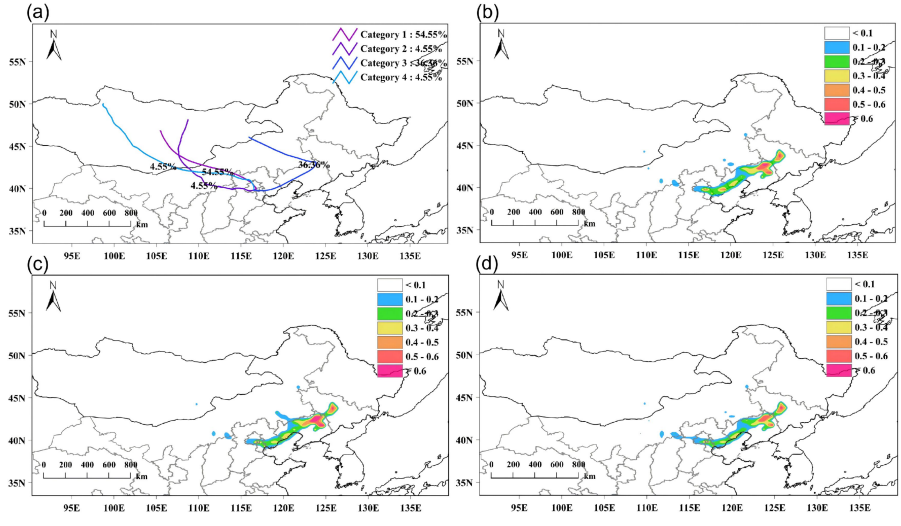

Figure 10. Backward trajectory clustering and PSCF analysis for the locally dominated episode. (a) Clusters of 72 h backward trajectories, where different colors indicate different trajectory types and percentages indicate the proportion of each trajectory type. (b, c, d) Spatial distributions of PSCF in 2016, 2030, and 2060, respectively, calculated based on the external transport contribution.

Table 3. Local emission and external transport contributions in the BTH region during the locally dominated episode.

https://doi.org/10.5194/egusphere-2026-3527
Preprint. Discussion started: 9 July 2026

Year	Local contribution (ppm)	External transport contribution (ppm)	Local fraction (%)	External transport fraction (%)	Local-to-transport ratio
2016	13.92	5.45	71.86%	28.14%	2.55
2030	21.34	6.86	75.67%	24.33%	3.11
2060	6.30	0.95	86.90%	13.10%	6.63

3.5.2 Transport-dominated episode

During the 26 to 28 January episode, anthropogenic CO_2 concentrations in the BTH region were dominated by external regional transport. Figures 11a and d show that high anthropogenic CO_2 values in 2016 and 2030 occurred within the BTH region and were also widely distributed over Shandong, Henan, Liaoning, and surrounding areas of North China. In Fig. 11b, e, and h, the near-surface wind fields formed a clear transport pathway over the BTH region and its surroundings. Airflow entered the BTH region from the west to northwest and then moved southward, producing high anthropogenic CO_2 contributions near the receptor region. Table 4 shows that the external transport contribution in 2016 was 9.84 ppm, much higher than the local contribution of 2.19 ppm, with an external transport fraction of 81.80%. In 2030, the external transport contribution increased to 15.69 ppm, accounting for 83.46%. In 2060, the external transport contribution decreased to 4.09 ppm, although its fraction remained high at 84.16%. These results indicate that external

https://doi.org/10.5194/egusphere-2026-3527
Preprint. Discussion started: 9 July 2026

720 regional transport can dominate anthropogenic CO_2 enhancement in the
721 BTH region under favorable transport conditions.

722 Figure 12 shows that this transport-dominated episode had a clearer
723 upstream pathway. The backward trajectories mainly entered the BTH
724 region from the west to northwest. The PSCF high-value regions showed
725 a band-shaped distribution from central Inner Mongolia, northern Shanxi,
726 and northern Hebei to the BTH region. These areas were important
727 potential source regions affecting high anthropogenic CO_2 values in
728 Beijing. In 2030, the PSCF high-value belt became more continuous,
729 suggesting that under enhanced emissions along the transport corridor in
730 the carbon peaking scenario, high external transport events were more
731 likely to occur along this pathway. In 2060, PSCF still indicated a similar
732 pathway, but the external transport contribution in Table 4 decreased from
733 9.84 ppm in 2016 to 4.09 ppm. This indicates that emission reductions
734 substantially weakened the actual transport intensity under the same
735 meteorological pathway.

736 The comparison between the two episodes shows that high-CO_2
737 episodes in the BTH region had clear meteorological dependence and
738 distinct source structures. During the locally dominated episode, the local
739 contribution accounted for 71.86% to 86.90%, indicating that local
740 emission accumulation was the main source. During the
741 transport-dominated episode, the lower-level wind field formed a clearer

https://doi.org/10.5194/egusphere-2026-3527
Preprint. Discussion started: 9 July 2026

upstream inflow pathway, and the external regional contribution exceeded the local contribution. The emission pathway mainly changed the absolute contribution magnitude: the 2030 pathway amplified anthropogenic CO_2 contributions, whereas the 2060 pathway substantially weakened both local and external contributions. Meteorological transport conditions determined the relative roles of local accumulation and regional inflow. Therefore, evaluations of CO_2 concentration responses in key regions under the carbon peaking and carbon neutrality pathways should consider local emission reductions, coordinated mitigation in surrounding regions, and the modulation of anthropogenic CO_2 contributions by meteorological transport conditions.

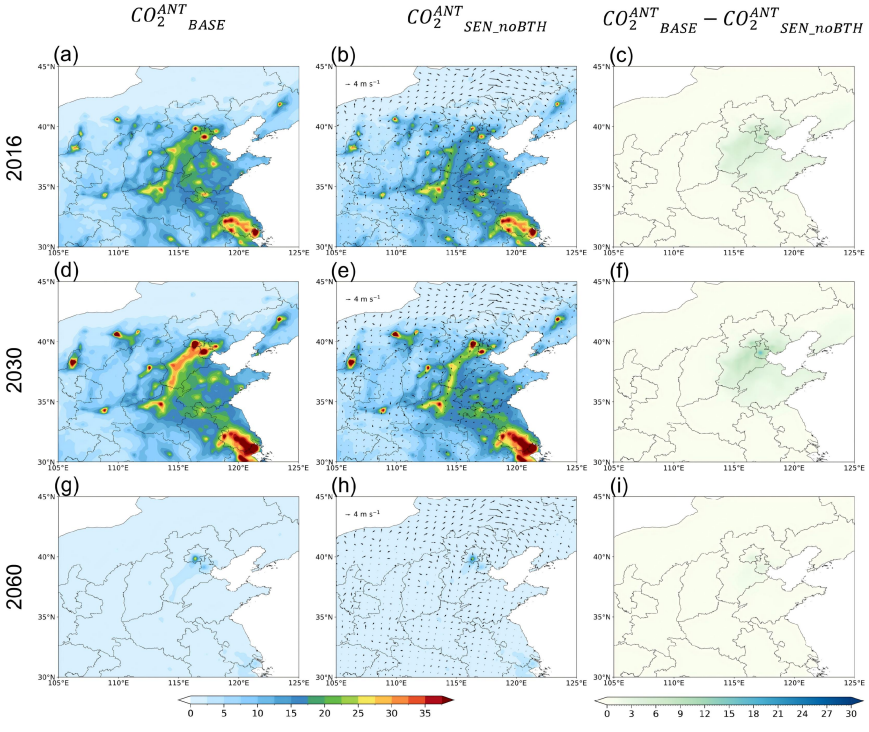

https://doi.org/10.5194/egusphere-2026-3527
Preprint. Discussion started: 9 July 2026

Figure 11. Decomposition of anthropogenic CO_2 contributions over the BTH region and surrounding areas during the transport-dominated episode. The panel settings are the same as in Fig. 9.

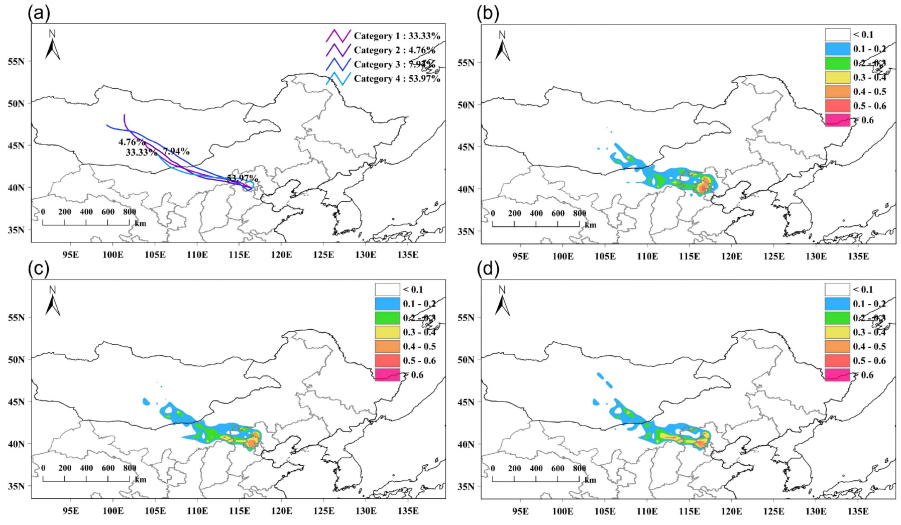

Figure 12. Backward trajectory clustering and PSCF analysis for the transport-dominated episode. The panel settings are the same as in Fig. 10.

Table 4. Local emission and external transport contributions in the BTH region during the transport-dominated episode.

Year	Local contribution (ppm)	External transport contribution (ppm)	Local fraction (%)	External transport fraction (%)	Local-to-transport ratio
2016	2.19	9.84	18.20%	81.80%	0.22
2030	3.11	15.69	16.54%	83.46%	0.20
2060	0.77	4.09	15.84%	84.16%	0.19

https://doi.org/10.5194/egusphere-2026-3527
Preprint. Discussion started: 9 July 2026

4. Discussion

4.1 Response of atmospheric CO_2 concentrations to the carbon peaking and carbon neutrality pathways

Studies of China's carbon peaking and carbon neutrality pathways have mainly focused on total emissions, energy structure, sectoral transitions, air quality improvement, and health benefits (Tong et al., 2020; Zhang and Chen, 2022a, b; Zhang et al., 2024; Zhou et al., 2024; Zhong et al., 2025). Building on these studies, this work examines how emission pathway changes translate into atmospheric concentration responses. The results show that the 2016, 2030, and 2060 emission pathways produced clear response signals in both surface CO_2 and XCO_2 over terrestrial China. Under the 2030 carbon peaking scenario, increased emissions led to a slight increase in CO_2 concentrations. Under the 2060 carbon neutrality scenario, deep emission reductions substantially weakened anthropogenic CO_2 enhancement.

The magnitude of the concentration response was much smaller than the magnitude of the emission change. This indicates that after emissions enter the atmosphere, the CO_2 concentration response is jointly regulated by background concentration, boundary-layer mixing, vertical dilution, horizontal transport, and biospheric fluxes. Previous studies have shown that the absolute median difference between screened and bias-corrected OCO-2 XCO_2 and TCCON measurements is less than 0.4 ppm, although

https://doi.org/10.5194/egusphere-2026-3527
Preprint. Discussion started: 9 July 2026

residual biases related to latitude, surface properties, and aerosol scattering remain (Wunch et al., 2017). Evaluations of satellite XCO_2 products such as OCO-2 and OCO-3 also indicate that the uncertainty and RMSE of satellite XCO_2 are often on the order of 0.7 to 1.1 ppm (Taylor et al., 2023; Fang et al., 2023). XCO_2 enhancements caused by regional fossil fuel emissions are generally weak, and the emission reduction signal in column concentrations may be only on the order of 0.1 to 0.2 ppm. It is therefore difficult to detect regional emission reductions directly using satellite XCO_2 alone (Buchwitz et al., 2021). In this study, the decrease in XCO_2 in 2060 was only 0.36 ppm, comparable to current satellite XCO_2 observational errors and regional systematic biases. High-resolution regional coupled models and contribution decomposition methods are therefore important for interpreting XCO_2 signals under deep emission reductions and for separating the anthropogenic and biospheric contributions to weak XCO_2 responses.

4.2 Complementary significance of surface CO_2 and XCO_2

Surface CO_2 and XCO_2 reflect CO_2 responses at different vertical scales. Surface CO_2 represents near-surface conditions and is more sensitive to local anthropogenic emissions, boundary-layer height, vertical mixing, and near-surface transport. It can therefore characterize emission accumulation and local variations near high-emission regions more directly. In this study, high surface CO_2 values mainly occurred in

https://doi.org/10.5194/egusphere-2026-3527
Preprint. Discussion started: 9 July 2026

anthropogenic emission-intensive regions, including the BTH region, Shandong, the Yangtze River Delta, the Pearl River Delta, and central urban agglomerations. These high values were slightly enhanced in 2030 and markedly weakened in 2060, indicating that surface CO_2 is suitable for diagnosing the effect of emission pathway changes on near-surface concentrations.

XCO_2 represents a column-averaged quantity over the full atmospheric column and has a smoother spatial distribution. Because XCO_2 is a pressure-weighted average over the atmospheric column, near-surface concentration signals are diluted during vertical mixing and column averaging. The attenuation factor further quantified this difference. The annual mean F_{att} values for 2030 and 2060 relative to 2016 were 0.179 and 0.188, respectively. Thus, only approximately 18% to 19% of the surface CO_2 change was reflected in XCO_2 on the annual mean scale. On the monthly scale, F_{att} ranged from 0.124 to 0.306 and from 0.142 to 0.294, respectively, indicating that this response conversion was also seasonally modulated by boundary-layer structure and vertical mixing.

Using surface CO_2 alone may overemphasize the influence of local emissions on the full atmospheric column, whereas using XCO_2 alone may underestimate the importance of near-surface emissions and boundary-layer processes. Combining surface CO_2 and XCO_2 allows

https://doi.org/10.5194/egusphere-2026-3527
Preprint. Discussion started: 9 July 2026

near-surface emission responses and regional-scale column responses to be identified simultaneously, making it more suitable for evaluating atmospheric CO_2 changes under the carbon peaking and carbon neutrality pathways.

4.3 Co-regulation of anthropogenic and biogenic contributions to the CO_2 response

The contribution decomposition results show that the anthropogenic contribution was the main source of CO_2 concentration differences among the emission pathways. In 2016 and 2030, the anthropogenic contribution was positive throughout the year and maintained relatively high CO_2 concentrations in winter and spring. After emissions reached their peak in 2030, the anthropogenic contribution increased, leading to a slight increase in CO_2 concentrations relative to 2016. By 2060, the anthropogenic contribution had decreased substantially, and the anthropogenic enhancement components in both surface CO_2 and XCO_2 were markedly weakened. This indicates that deep emission reductions can effectively reduce the atmospheric CO_2 enhancement caused by anthropogenic emissions.

The biogenic contribution mainly regulated the seasonal phase. In summer, enhanced vegetation photosynthesis increased CO_2 uptake by terrestrial ecosystems, causing the biogenic contribution to become negative and offsetting part of the anthropogenic enhancement. After the

https://doi.org/10.5194/egusphere-2026-3527
Preprint. Discussion started: 9 July 2026

transition to carbon neutrality, the regulatory mechanism of atmospheric CO_2 changed markedly. During the high-emission stage, CO_2 differences among scenarios were mainly controlled by anthropogenic emissions, while biospheric fluxes mainly modulated the seasonal phase. By the carbon neutrality stage, both the absolute anthropogenic contribution and its seasonal amplitude had decreased substantially, and the relative influence of terrestrial ecosystem uptake and release on monthly CO_2 variations increased. This result suggests that even if future biogenic fluxes remain at current levels, deep emission reductions will make ecosystem processes more prominent in regulating seasonal atmospheric CO_2 variations.

4.4 Influence of regional transport on high CO_2 episodes in key regions

The BTH case results show that the source composition of high-CO_2 episodes was strongly modulated by meteorology. Under weak-wind and stagnant conditions, local anthropogenic emissions accumulated within the boundary layer, making the local contribution the dominant source of anthropogenic CO_2 enhancement in the BTH region. The emission increase in 2030 amplified this local accumulation, whereas deep emission reductions in 2060 substantially reduced the absolute enhancement. Under favorable transport conditions, external regional transport could dominate anthropogenic CO_2 enhancement in the BTH

https://doi.org/10.5194/egusphere-2026-3527
Preprint. Discussion started: 9 July 2026

region. The backward trajectory and PSCF results show that transport pathways from the west to northwest can carry anthropogenic CO_2 from upstream source regions into the BTH region. Previous studies have also shown that weather systems, boundary-layer height, and regional circulation strongly affect CO_2 transport and accumulation (Chan et al., 2004; Hurwitz et al., 2004; Parazoo et al., 2011; Díaz-Isaac et al., 2014, 2018; Dong et al., 2021). This study further shows that emission pathways mainly changed the absolute magnitudes of the local and external transport contributions, while meteorological conditions determined their relative proportions.

This finding has implications for CO_2 assessment in key regions. For high-emission receptor regions such as the BTH region, local emission reductions can reduce near-surface accumulation during stagnant episodes, while coordinated mitigation in surrounding regions can weaken transport-dominated high-concentration episodes. Future assessments of CO_2 concentration changes in key regions should consider local emissions, upstream source regions, and meteorological transport conditions together. Otherwise, the influence of external transport on high-concentration episodes may be underestimated, and changes in source composition under different weather patterns may be overlooked.

4.5 Uncertainties and future work

This study used the same meteorological background, CO_2 initial

https://doi.org/10.5194/egusphere-2026-3527
Preprint. Discussion started: 9 July 2026

and boundary conditions, vegetation indices, and VPRM parameters, and changed only the anthropogenic emission inputs. This design helps isolate the concentration responses caused by emission pathway changes. In real future scenarios, however, the climate background, boundary-layer structure, wind fields, temperature, moisture conditions, vegetation activity, and background CO_2 concentrations may all change. The results of this study are therefore best interpreted as sensitivity responses to anthropogenic emissions under a fixed meteorological and ecological background. Future studies should incorporate changes in climate, land cover, and ecosystem responses to evaluate CO_2 concentration changes under conditions closer to the real future atmosphere.

Biogenic fluxes are an important source of uncertainty. VPRM estimates ecosystem CO_2 exchange using satellite vegetation indices, temperature, water stress functions, and empirical parameters. Using fixed 2016 vegetation indices and VPRM parameters helps highlight the influence of anthropogenic emission changes, but it does not fully account for future ecosystem feedbacks to environmental change. Therefore, the enhanced relative role of biospheric fluxes in 2060 should be interpreted as a sensitivity result under fixed biogenic flux conditions. In the real future, CO_2 fertilization, nitrogen deposition, and phenological changes may enhance vegetation carbon uptake, while climate stress, drought, and high temperature may weaken carbon sinks and enhance

https://doi.org/10.5194/egusphere-2026-3527
Preprint. Discussion started: 9 July 2026

ecosystem respiration. These processes could alter the seasonal amplitude and regional differences in the biogenic contribution. Future studies should couple WRF-VPRM with dynamic vegetation models, future land-use scenarios, and climate change scenarios to further evaluate the influence of changes in biospheric fluxes on regional CO_2 concentrations during the carbon neutrality stage.

Model validation also has limitations. This study mainly used the Mapping-XCO_2 dataset to validate the seasonal variation of XCO_2 over China in 2016. This evaluation indicates that the model can reasonably reproduce the overall variation in column concentrations, but constraints on surface CO_2, boundary-layer height, vertical profiles, and biogenic fluxes remain limited. Future studies could conduct multi-scale validation using flux towers, ground-based CO_2 sites, tower-based profile observations, TCCON-like column concentration data, and additional satellite products. The BTH regional analysis selected two typical episodes, which helped reveal local accumulation and regional transport mechanisms. However, these cases cannot represent all high-CO_2 episodes throughout the year. Future work could be extended to multi-year classification of high-concentration episodes, with statistics on the frequency, intensity, and transport pathways of local and external contributions under different weather patterns. Seasonal differences in transport should also be examined to provide a more comprehensive

https://doi.org/10.5194/egusphere-2026-3527
Preprint. Discussion started: 9 July 2026

assessment of CO_2 responses in key regions under the carbon peaking and carbon neutrality pathways.

5. Conclusions

Based on WRF-VPRM, this study designed a 2016 baseline emission scenario, a 2030 carbon peaking scenario, and a 2060 carbon neutrality scenario to analyze the responses of surface CO_2 and XCO_2 over terrestrial China to different emission pathways. The sources of CO_2 concentration changes were identified by decomposing the background, biogenic, and anthropogenic components. The simulated XCO_2 in 2016 agreed well with the Mapping-XCO_2 dataset, with an R of 0.986, an MB of 0.776 ppm, and an RMSE of 0.942 ppm. This indicates that the model configuration can reasonably reproduce the main seasonal variations in XCO_2 over China and supports the scenario analysis.

CO_2 concentrations over terrestrial China showed clear responses to the carbon peaking and carbon neutrality emission pathways. Under the 2030 carbon peaking scenario, surface CO_2 and XCO_2 increased by 0.363 and 0.065 ppm relative to 2016, respectively. Under the 2060 carbon neutrality scenario, they decreased by 1.914 and 0.359 ppm, respectively. Surface CO_2 was more sensitive to emission changes, while the XCO_2 response was smaller and spatially smoother. The 0.359 ppm XCO_2 decrease in 2060 was comparable to current satellite XCO_2 observational errors and regional systematic biases, indicating that direct detection of

https://doi.org/10.5194/egusphere-2026-3527
Preprint. Discussion started: 9 July 2026

regional deep-mitigation signals using satellite column concentrations alone remains challenging. The attenuation factor showed that only approximately 17.9% to 18.8% of the surface CO_2 change was reflected in XCO_2 on the annual mean scale, indicating a clear dilution effect of column averaging on near-surface concentrations. High-resolution regional coupled models and tracer-component decomposition are therefore important for identifying weak XCO2 emission signals and attributing them to anthropogenic and biospheric contributions.

The contribution decomposition results showed that the anthropogenic contribution controlled the main concentration differences among the emission pathways, while the biogenic contribution mainly shaped seasonal variations. In 2016 and 2030, anthropogenic emissions remained the main source of CO_2 enhancement in winter and spring. By 2060, the anthropogenic contribution decreased substantially, and the seasonal amplitudes of the anthropogenic component in surface CO_2 and XCO_2 decreased to 0.17 and 0.04 ppm, respectively, while the biogenic amplitude remained nearly unchanged. This indicates that after the transition to the deep-mitigation stage, seasonal variations in atmospheric CO_2 will be shaped mainly by terrestrial ecosystem exchange, while still being affected by residual anthropogenic emissions.

The BTH sensitivity experiments showed that the source composition of high-CO_2 episodes in key regions was strongly affected

https://doi.org/10.5194/egusphere-2026-3527
Preprint. Discussion started: 9 July 2026

by meteorological conditions. Under weak-wind and stagnant conditions, local emission accumulation dominated anthropogenic CO_2 enhancement, with local fractions of 71.86%, 75.67%, and 86.90% in 2016, 2030, and 2060, respectively. Under favorable transport conditions, external regional transport became the main contributor, with fractions of 81.80%, 83.46%, and 84.16%, respectively. Increased emissions in 2030 amplified both local accumulation and regional transport contributions, whereas deep emission reductions in 2060 weakened their absolute magnitudes. These results indicate that CO_2 concentration responses in key regions cannot be evaluated from emissions within administrative boundaries alone. Upstream source regions and meteorological transport processes also need to be considered.

Overall, this study establishes a quantitative link between China's carbon peaking and carbon neutrality emission pathways and atmospheric CO_2 responses. It also reveals how anthropogenic emissions, biospheric fluxes, and regional transport jointly regulate CO_2 variations. The results suggest that emission inventories, regional models, satellite XCO_2, and ground-based CO_2 observations should be integrated when evaluating the atmospheric CO_2 responses of the carbon peaking and carbon neutrality pathways. Such integration can help distinguish the relative contributions of anthropogenic mitigation, biospheric carbon sinks, and transport processes. For high-emission receptor regions such as the BTH region,

https://doi.org/10.5194/egusphere-2026-3527
Preprint. Discussion started: 9 July 2026

both local emission reductions and coordinated mitigation in surrounding regions are important for reducing high anthropogenic CO_2 episodes.

Data availability

The processed data supporting the figures, tables, and main conclusions of this study are publicly available from Zenodo at https://doi.org/10.5281/zenodo.20698486 (Gu et al., 2026). The archive contains processed gridded fields, time series, vertical profiles, model-based contribution diagnostics, BTH case-study data, receptor-point data for PSCF analysis, HYSPLIT meteorological driving files, and tabulated statistics used in the manuscript. The original third-party datasets are not redistributed in the Zenodo archive and remain available from their respective data providers. The Mapping-XCO2 dataset (Sheng et al., 2023) is available from Harvard Dataverse at https://dataverse.harvard.edu/dataset.xhtml?persistentId=doi:10.7910/DVN/4WDTD8. The NCEP ADP Global Surface Observational Weather Data (National Centers for Environmental Prediction et al., 2008) are available from the NCAR Research Data Archive at https://gdex.ucar.edu/datasets/d461000/dataaccess/. ERA5 reanalysis data (Hersbach et al., 2020) are available from the Copernicus Climate Data Store at https://cds.climate.copernicus.eu/datasets/reanalysis-era5-pressure-levels?tab=download. CAMS greenhouse gas products (Copernicus Atmosphere Monitoring Service, 2020) are available from the Copernicus At

https://doi.org/10.5194/egusphere-2026-3527
Preprint. Discussion started: 9 July 2026

mosphere Data Store at https://ads.atmosphere.copernicus.eu/datasets/cams-global-greenhouse-gas-inversion?tab=download. The MEIC emission inventory (Xu et al., 2023; Geng et al., 2024) is available at http://meicmodel.org.cn/?page_id=2345, and the DPEC emission scenarios (Tong et al., 2020; Cheng et al., 2023) are available at http://meicmodel.org.cn/?page_id=1917.

Author contribution

Kaiqiang Gu conceptualized the study, developed the methodology, performed the investigation and formal analysis, curated the data, produced the visualizations, and wrote the original draft. Yi Yang contributed to conceptualization, formal analysis, supervision, funding acquisition, and manuscript review and editing. Xiaoming Hu contributed to conceptualization, supervision, and manuscript review and editing. Shixiang Su contributed to formal analysis and manuscript review and editing. Feifan Bian contributed to manuscript review and editing. All authors reviewed and approved the final manuscript.

Competing interests

The authors declare that they have no conflict of interest.

Acknowledgements

The authors acknowledge the Supercomputing Center of Lanzhou University for providing computational resources.

Financial support

https://doi.org/10.5194/egusphere-2026-3527
Preprint. Discussion started: 9 July 2026

This work was supported by the National Natural Science Foundation of China (grant no. 42275162).

References

Ahmadov, R., Gerbig, C., Kretschmer, R., Koerner, S., Neininger, B., Dolman, A. J., and Sarrat, C.: Mesoscale covariance of transport and CO2 fluxes: Evidence from observations and simulations using the WRF-VPRM coupled atmosphere-biosphere model, J. Geophys. Res.-Atmos., 112, D22107, https://doi.org/10.1029/2007JD008552, 2007.

Ahmadov, R., Gerbig, C., Kretschmer, R., Körner, S., Rödenbeck, C., Bousquet, P., and Ramonet, M.: Comparing high resolution WRF-VPRM simulations and two global CO2 transport models with coastal tower measurements of CO2, Biogeosciences, 6, 807–817, https://doi.org/10.5194/bg-6-807-2009, 2009.

Ashbaugh, L. L., Malm, W. C., and Sadeh, W. Z.: A residence time probability analysis of sulfur concentrations at Grand Canyon National Park, Atmos. Environ., 19, 1263–1270, https://doi.org/10.1016/0004-6981(85)90256-2, 1985.

Buchwitz, M., Reuter, M., Noël, S., Bramstedt, K., Schneising, O., Hilker, M., Fuentes Andrade, B., Bovensmann, H., Burrows, J. P., Di Noia, A., Boesch, H., Wu, L., Landgraf, J., Aben, I., Retscher, C., O'Dell, C. W., and Crisp, D.: Can a regional-scale reduction of atmospheric CO2 during the COVID-19 pandemic be detected from space? A case study for East China using satellite XCO2 retrievals, Atmos. Meas. Tech., 14, 2141–2166, https://doi.org/10.5194/amt-14-2141-2021, 2021.

Cai, B., Liang, S., Zhou, J., Wang, J., Cao, L., Qu, S., Xu, M., and Yang, Z.: China high resolution emission database (CHRED) with point emission sources, gridded emission data, and supplementary socioeconomic data, Resour. Conserv. Recycl., 129, 232–239, https://doi.org/10.1016/j.resconrec.2017.10.036, 2018.

Canadell, J. G., Monteiro, P. M. S., Costa, M. H., Cotrim da Cunha, L., Cox, P. M., Eliseev, A. V., Henson, S., Ishii, M., Jaccard, S., Koven, C., Lohila, A., Patra, P. K., Piao, S., Rogelj, J., Syampungani, S., Zaehle, S., and Zickfeld, K.: Global carbon and other biogeochemical cycles and feedbacks, in: Climate Change 2021: The Physical Science Basis, edited by: Masson-Delmotte, V., Zhai, P., Pirani, A., Connors, S. L., Péan, C., Berger, S., Caud, N., Chen, Y., Goldfarb, L., Gomis, M. I., Huang, M., Leitzell, K., Lonnoy, E., Matthews, J. B. R., Maycock, T. K., Waterfield, T., Yelekçi, O., Yu, R., and Zhou, B., Cambridge University Press, Cambridge, United Kingdom and New York, NY, USA, 673–816, https://doi.org/10.1017/9781009157896.007, 2021.

Chan, D., Yuen, C. W., Higuchi, K., Shashkov, A., Liu, J., Chen, J., and Worthy, D.: On the CO2 exchange between the atmosphere and the biosphere: the role of synoptic and mesoscale processes, Tellus B, 56, 194–212, https://doi.org/10.1111/j.1600-0889.2004.00104.x, 2004.

https://doi.org/10.5194/egusphere-2026-3527
Preprint. Discussion started: 9 July 2026

Chen, S.-H. and Sun, W.-Y.: A one-dimensional time dependent cloud model, J. Meteorol. Soc. Jpn., 80, 99–118, https://doi.org/10.2151/jmsj.80.99, 2002.

Chen, X., He, Q., Ye, T., Liang, Y., and Li, Y.: Decoding spatiotemporal dynamics in atmospheric CO2 in Chinese cities: Insights from satellite remote sensing and geographically and temporally weighted regression analysis, Sci. Total Environ., 908, 167917, https://doi.org/10.1016/j.scitotenv.2023.167917, 2024.

Cheng, J., Tong, D., Liu, Y., Geng, G., Davis, S. J., He, K., and Zhang, Q.: A synergistic approach to air pollution control and carbon neutrality in China can avoid millions of premature deaths annually by 2060, One Earth, 6, 978–989, https://doi.org/10.1016/j.oneear.2023.07.007, 2023.

Ciais, P., Sabine, C., Bala, G., Bopp, L., Brovkin, V., Canadell, J. G., Chhabra, A., DeFries, R., Galloway, J., Heimann, M., Jones, C., Le Quéré, C., Myneni, R. B., Piao, S., and Thornton, P.: Carbon and other biogeochemical cycles, in: Climate Change 2013: The Physical Science Basis, edited by: Stocker, T. F., Qin, D., Plattner, G.-K., Tignor, M., Allen, S. K., Boschung, J., Nauels, A., Xia, Y., Bex, V., and Midgley, P. M., Cambridge University Press, Cambridge, United Kingdom and New York, NY, USA, 465–570, https://doi.org/10.1017/CBO9781107415324.015, 2013.

Copernicus Atmosphere Monitoring Service: CAMS global inversion-optimised greenhouse gas fluxes and concentrations, Atmosphere Data Store [data set], https://doi.org/10.24381/ed2851d2, 2020.

Crisp, D., Atlas, R. M., Bréon, F.-M., Brown, L. R., Burrows, J. P., Ciais, P., Connor, B. J., Doney, S. C., Fung, I. Y., Jacob, D. J., Miller, C. E., O'Brien, D., Pawson, S., Randerson, J. T., Rayner, P., Salawitch, R. J., Sander, S. P., Sen, B., Stephens, G. L., Tans, P. P., Toon, G. C., Wennberg, P. O., Wofsy, S. C., Yung, Y. L., Kuang, Z., Chudasama, B., Sprague, G., Weiss, B., Pollock, R., Kenyon, D., and Schroll, S.: The Orbiting Carbon Observatory (OCO) mission, Adv. Space Res., 34, 700–709, https://doi.org/10.1016/j.asr.2003.08.062, 2004.

Díaz-Isaac, L. I., Lauvaux, T., Davis, K. J., Miles, N. L., Richardson, S. J., Jacobson, A. R., and Andrews, A. E.: Model-data comparison of MCI field campaign atmospheric CO2 mole fractions, J. Geophys. Res.-Atmos., 119, 10536–10551, https://doi.org/10.1002/2014JD021593, 2014.

Díaz-Isaac, L. I., Lauvaux, T., and Davis, K. J.: Impact of physical parameterizations and initial conditions on simulated atmospheric transport and CO2 mole fractions in the US Midwest, Atmos. Chem. Phys., 18, 14813–14835, https://doi.org/10.5194/acp-18-14813-2018, 2018.

Dong, X., Yue, M., Jiang, Y., Hu, X.-M., Ma, Q., Pu, J., and Zhou, G.: Analysis of CO2 spatio-temporal variations in China using a weather-biosphere online coupled model, Atmos. Chem. Phys., 21, 7217–7233, https://doi.org/10.5194/acp-21-7217-2021, 2021.

Eldering, A., Wennberg, P. O., Crisp, D., Schimel, D. S., Gunson, M. R., Chatterjee, A., Liu, J., Schwandner, F. M., Sun, Y., O'Dell, C. W., Frankenberg, C., Taylor, T. E., Fisher, B., Osterman, G. B., Wunch, D., Hakkarainen, J., Tamminen, J., and Weir, B.: The Orbiting Carbon Observatory-2 early science investigations of

https://doi.org/10.5194/egusphere-2026-3527
Preprint. Discussion started: 9 July 2026

regional carbon dioxide fluxes, Science, 358, eaam5745, https://doi.org/10.1126/science.aam5745, 2017.

Fang, J., Chen, B., Zhang, H., Dilawar, A., Guo, M., Liu, C., Liu, S., Gemechu, T. M., and Zhang, X.: Global evaluation and intercomparison of XCO2 retrievals from GOSAT, OCO-2, and TANSAT with TCCON, Remote Sens., 15, 5073, https://doi.org/10.3390/rs15205073, 2023.

Feng, S., Lauvaux, T., Newman, S., Rao, P., Ahmadov, R., Deng, A., Díaz-Isaac, L. I., Duren, R. M., Fischer, M. L., Gerbig, C., Gurney, K. R., Huang, J., Jeong, S., Li, Z., Miller, C. E., O'Keeffe, D., Patarasuk, R., Sander, S. P., Song, Y., Wong, K. W., and Yung, Y. L.: Los Angeles megacity: a high-resolution land-atmosphere modelling system for urban CO2 emissions, Atmos. Chem. Phys., 16, 9019–9045, https://doi.org/10.5194/acp-16-9019-2016, 2016.

Friedlingstein, P., O'Sullivan, M., Jones, M. W., Andrew, R. M., Hauck, J., Landschützer, P., Le Quéré, C., Li, H., Luijkx, I. T., Olsen, A., Peters, G. P., Peters, W., Pongratz, J., Schwingshackl, C., Sitch, S., Canadell, J. G., Ciais, P., Jackson, R. B., Alin, S. R., Arneth, A., Arora, V., Bates, N. R., Becker, M., Bellouin, N., Berghoff, C. F., Bittig, H. C., Bopp, L., Cadule, P., Campbell, K., Chamberlain, M. A., Chandra, N., Chevallier, F., Chini, L. P., Colligan, T., Decayeux, J., Djeutchouang, L. M., Dou, X., Duran Rojas, C., Enyo, K., Evans, W., Fay, A. R., Feely, R. A., Ford, D. J., Foster, A., Gasser, T., Gehlen, M., Gkritzalis, T., Grassi, G., Gregor, L., Gruber, N., Gürses, Ö., Harris, I., Hefner, M., Heinke, J., Hurtt, G. C., Iida, Y., Ilyina, T., Jacobson, A. R., Jain, A. K., Jarníková, T., Jersild, A., Jiang, F., Jin, Z., Kato, E., Keeling, R. F., Klein Goldewijk, K., Knauer, J., Korsbakken, J. I., Lan, X., Lauvset, S. K., Lefèvre, N., Liu, Z., Liu, J., Ma, L., Maksyutov, S., Marland, G., Mayot, N., McGuire, P. C., Metzl, N., Monacci, N. M., Morgan, E. J., Nakaoka, S.-I., Neill, C., Niwa, Y., Nützel, T., Olivier, L., Ono, T., Palmer, P. I., Pierrot, D., Qin, Z., Resplandy, L., Roobaert, A., Rosan, T. M., Rödenbeck, C., Schwinger, J., Smallman, T. L., Smith, S. M., Sospedra-Alfonso, R., Steinhoff, T., Sun, Q., Sutton, A. J., Séférian, R., Takao, S., Tatebe, H., Tian, H., Tilbrook, B., Torres, O., Tourigny, E., Tsujino, H., Tubiello, F., van der Werf, G., Wanninkhof, R., Wang, X., Yang, D., Yang, X., Yu, Z., Yuan, W., Yue, X., Zaehle, S., Zeng, N., and Zeng, J.: Global Carbon Budget 2024, Earth Syst. Sci. Data, 17, 965–1039, https://doi.org/10.5194/essd-17-965-2025, 2025.

Geng, G., Liu, Y., Liu, Y., Liu, S., Cheng, J., Yan, L., Wu, N., Hu, H., Tong, D., Zheng, B., Yin, Z., He, K., and Zhang, Q.: Efficacy of China's clean air actions to tackle PM2.5 pollution between 2013 and 2020, Nat. Geosci., 17, 987–994, https://doi.org/10.1038/s41561-024-01540-z, 2024.

Grell, G. A.: Prognostic evaluation of assumptions used by cumulus parameterizations, Mon. Weather Rev., 121, 764–787, https://doi.org/10.1175/1520-0493(1993)121<0764:PEOAUB>2.0.CO;2, 1993.

Grell, G. A. and Dévényi, D.: A generalized approach to parameterizing convection combining ensemble and data assimilation techniques, Geophys. Res. Lett., 29, 1693, https://doi.org/10.1029/2002GL015311, 2002.

https://doi.org/10.5194/egusphere-2026-3527
Preprint. Discussion started: 9 July 2026

Gu, K., Yang, Y., Su, S., Hu, X., and Bian, F.: Data for "Contrasting surface and column-averaged CO2 responses over terrestrial China under carbon peaking and carbon neutrality emission pathways: anthropogenic, biospheric, and regional transport contributions", version 1.0, Zenodo [data set], https://doi.org/10.5281/zenodo.20698486, 2026.

Hersbach, H., Bell, B., Berrisford, P., Hirahara, S., Horányi, A., Muñoz-Sabater, J., Nicolas, J., Peubey, C., Radu, R., Schepers, D., Simmons, A., Soci, C., Abdalla, S., Abellan, X., Balsamo, G., Bechtold, P., Biavati, G., Bidlot, J., Bonavita, M., De Chiara, G., Dahlgren, P., Dee, D., Diamantakis, M., Dragani, R., Flemming, J., Forbes, R., Fuentes, M., Geer, A., Haimberger, L., Healy, S., Hogan, R. J., Hólm, E., Janisková, M., Keeley, S., Laloyaux, P., Lopez, P., Lupu, C., Radnoti, G., de Rosnay, P., Rozum, I., Vamborg, F., Villaume, S., and Thépaut, J.-N.: The ERA5 global reanalysis, Q. J. Roy. Meteor. Soc., 146, 1999–2049, https://doi.org/10.1002/qj.3803, 2020.

Hong, S.-Y., Noh, Y., and Dudhia, J.: A new vertical diffusion package with an explicit treatment of entrainment processes, Mon. Weather Rev., 134, 2318–2341, https://doi.org/10.1175/MWR3199.1, 2006.

Hu, X.-M., Crowell, S., Wang, Q., Zhang, Y., Davis, K. J., Xue, M., Xiao, X., Moore, B., Wu, X., Choi, Y., and DiGangi, J. P.: Dynamical downscaling of CO2 in 2016 over the contiguous United States using WRF-VPRM, a weather-biosphere-online-coupled model, J. Adv. Model. Earth Syst., 12, e2019MS001875, https://doi.org/10.1029/2019MS001875, 2020.

Hu, X.-M., Hu, J., Gao, L., Cai, C., Jiang, Y., Xue, M., and Wang, S.: Multisensor and multimodel monitoring and investigation of a wintertime air pollution event ahead of a cold front over eastern China, J. Geophys. Res.-Atmos., 126, e2020JD033538, https://doi.org/10.1029/2020JD033538, 2021.

Hurwitz, M. D., Ricciuto, D. M., Bakwin, P. S., Davis, K. J., Wang, W., Yi, C., and Butler, M. P.: Transport of carbon dioxide in the presence of storm systems over a northern Wisconsin forest, J. Atmos. Sci., 61, 607–618, https://doi.org/10.1175/1520-0469(2004)061<0607:TOCDIT>2.0.CO;2, 2004.

International Energy Agency (IEA): An Energy Sector Roadmap to Carbon Neutrality in China, IEA, Paris, 2021.

Le Quéré, C., Andrew, R. M., Friedlingstein, P., Sitch, S., Hauck, J., Pongratz, J., Pickers, P. A., Korsbakken, J. I., Peters, G. P., Canadell, J. G., Arneth, A., Arora, V. K., Barbero, L., Bastos, A., Bopp, L., Chevallier, F., Chini, L. P., Ciais, P., Doney, S. C., Gkritzalis, T., Goll, D. S., Harris, I., Haverd, V., Hoffman, F. M., Hoppema, M., Houghton, R. A., Hurtt, G., Ilyina, T., Jain, A. K., Johannessen, T., Jones, C. D., Kato, E., Keeling, R. F., Klein Goldewijk, K., Landschützer, P., Lefèvre, N., Lienert, S., Liu, Z., Lombardozzi, D., Metzl, N., Munro, D. R., Nabel, J. E. M. S., Nakaoka, S.-I., Neill, C., Olsen, A., Ono, T., Patra, P., Peregon, A., Peters, W., Peylin, P., Pfeil, B., Pierrot, D., Poulter, B., Rehder, G., Resplandy, L., Robertson, E., Rocher, M., Rödenbeck, C., Schuster, U., Schwinger, J., Séférian, R., Skjelvan, I., Steinhoff, T., Sutton, A., Tans, P. P., Tian, H., Tilbrook, B., Tubiello, F. N., van der Laan-Luijkx, I. T., van der Werf,

https://doi.org/10.5194/egusphere-2026-3527
Preprint. Discussion started: 9 July 2026

G. R., Viovy, N., Walker, A. P., Wiltshire, A. J., Wright, R., Zaehle, S., and Zheng, B.: Global Carbon Budget 2018, Earth Syst. Sci. Data, 10, 2141–2194, https://doi.org/10.5194/essd-10-2141-2018, 2018.

Li, X., Hu, X.-M., Cai, C., Jia, Q., Zhang, Y., Liu, J., and Feng, S.: Terrestrial CO2 fluxes, concentrations, sources and budget in Northeast China: Observational and modeling studies, J. Geophys. Res.-Atmos., 125, e2019JD031686, https://doi.org/10.1029/2019JD031686, 2020.

Mahadevan, P., Wofsy, S. C., Matross, D. M., Xiao, X., Dunn, A. L., Lin, J. C., Gerbig, C., Munger, J. W., Chow, V. Y., and Gottlieb, E. W.: A satellite-based biosphere parameterization for net ecosystem CO2 exchange: Vegetation Photosynthesis and Respiration Model (VPRM), Global Biogeochem. Cy., 22, GB2005, https://doi.org/10.1029/2006GB002735, 2008.

National Centers for Environmental Prediction, National Weather Service, NOAA, and U.S. Department of Commerce: NCEP ADP Global Upper Air and Surface Weather Observations (PREPBUFR format), NSF National Center for Atmospheric Research [data set], https://doi.org/10.5065/Z83F-N512, 2008.

Neale, R. B., Richter, J. H., Conley, A. J., Park, S., Lauritzen, P. H., Gettelman, A., Williamson, D. L., Rasch, P. J., Vavrus, S. J., Taylor, M. A., Collins, W. D., Zhang, M., and Lin, S.-J.: Description of the NCAR Community Atmosphere Model (CAM 4.0), NCAR Technical Note, NCAR/TN-485+STR, National Center for Atmospheric Research, Boulder, CO, USA, https://doi.org/10.5065/GSEB-6470, 2010.

O'Dell, C. W., Connor, B., Bösch, H., O'Brien, D., Frankenberg, C., Castano, R., Christi, M., Eldering, D., Fisher, B., Gunson, M., McDuffie, J., Miller, C. E., Natraj, V., Oyafuso, F., Polonsky, I., Smyth, M., Taylor, T., Toon, G. C., Wennberg, P. O., and Wunch, D.: The ACOS CO2 retrieval algorithm, Part 1: Description and validation against synthetic observations, Atmos. Meas. Tech., 5, 99–121, https://doi.org/10.5194/amt-5-99-2012, 2012.

Parazoo, N. C., Denning, A. S., Berry, J. A., Wolf, A., Randall, D. A., Kawa, S. R., Pauluis, O., and Doney, S. C.: Moist synoptic transport of CO2 along the mid-latitude storm track, Geophys. Res. Lett., 38, L09804, https://doi.org/10.1029/2011GL047238, 2011.

Park, C., Gerbig, C., Newman, S., Ahmadov, R., Feng, S., Gurney, K. R., Carmichael, G. R., Park, S.-Y., Lee, H.-W., Goulden, M., Stutz, J., Peischl, J., and Ryerson, T.: CO2 transport, variability, and budget over the Southern California Air Basin using the high-resolution WRF-VPRM model during the CalNex 2010 campaign, J. Appl. Meteorol. Clim., 57, 1337–1352, https://doi.org/10.1175/JAMC-D-17-0358.1, 2018.

Pillai, D., Gerbig, C., Kretschmer, R., Beck, V., Karstens, U., Neininger, B., and Heimann, M.: Comparing Lagrangian and Eulerian models for CO2 transport: A step towards Bayesian inverse modeling using WRF/STILT-VPRM, Atmos. Chem. Phys., 12, 8979–8991, https://doi.org/10.5194/acp-12-8979-2012, 2012.

https://doi.org/10.5194/egusphere-2026-3527
Preprint. Discussion started: 9 July 2026

Rolph, G., Stein, A., and Stunder, B.: Real-time Environmental Applications and Display sYstem: READY, Environ. Modell. Softw., 95, 210–228, https://doi.org/10.1016/j.envsoft.2017.06.025, 2017.

Sheng, M., Lei, L., Zeng, Z.-C., Rao, W., Ran, L., Zhang, B., Lin, X., and Liang, A.: Global land 1° mapping dataset of XCO2 from satellite observations of GOSAT and OCO-2 from 2009 to 2020, Big Earth Data, 7, 170–190, https://doi.org/10.1080/20964471.2022.2033149, 2023.

Sheng, M., Hou, Y., Song, H., Ye, X., Lei, L., Ma, P., and Zeng, Z.-C.: Estimating anthropogenic CO2 emissions from China's Yangtze River Delta using OCO-2 observations and WRF-Chem simulations, Remote Sens. Environ., 316, 114515, https://doi.org/10.1016/j.rse.2024.114515, 2025.

Stauffer, D. R. and Seaman, N. L.: Use of four-dimensional data assimilation in a limited-area mesoscale model. Part I: Experiments with synoptic-scale data, Mon. Weather Rev., 118, 1250–1277, https://doi.org/10.1175/1520-0493(1990)118<1250:UOFDDA>2.0.CO;2, 1990.

Stauffer, D. R. and Seaman, N. L.: Multiscale four-dimensional data assimilation, J. Appl. Meteorol., 33, 416–434, https://doi.org/10.1175/1520-0450(1994)033<0416:MFDDA>2.0.CO;2, 1994.

Stein, A. F., Draxler, R. R., Rolph, G. D., Stunder, B. J. B., Cohen, M. D., and Ngan, F.: NOAA's HYSPLIT atmospheric transport and dispersion modeling system, Bull. Amer. Meteor. Soc., 96, 2059–2077, https://doi.org/10.1175/BAMS-D-14-00110.1, 2015.

Taylor, T. E., O'Dell, C. W., Baker, D., Bruegge, C., Chang, A., Chapsky, L., Chatterjee, A., Cheng, C., Chevallier, F., Crisp, D., Dang, L., Drouin, B., Eldering, A., Feng, L., Fisher, B., Fu, D., Gunson, M., Haemmerle, V., Keller, G. R., Kiel, M., Kuai, L., Kurosu, T., Lambert, A., Laughner, J., Lee, R., Liu, J., Mandrake, L., Marchetti, Y., McGarragh, G., Merrelli, A., Nelson, R. R., Osterman, G., Oyafuso, F., Palmer, P. I., Payne, V. H., Rosenberg, R., Somkuti, P., Spiers, G., To, C., Weir, B., Wennberg, P. O., Yu, S., and Zong, J.: Evaluating the consistency between OCO-2 and OCO-3 XCO2 estimates derived from the NASA ACOS version 10 retrieval algorithm, Atmos. Meas. Tech., 16, 3173–3209, https://doi.org/10.5194/amt-16-3173-2023, 2023.

Tewari, M., Wang, W., Dudhia, J., and LeMone, M. A.: Implementation and verification of the unified NOAH land surface model in the WRF model, 20th Conference on Weather Analysis and Forecasting and 16th Conference on Numerical Weather Prediction, Seattle, WA, USA, American Meteorological Society, 11–15 January 2004, 2004.

Tong, D., Cheng, J., Liu, Y., Yu, S., Yan, L., Hong, C., Qin, Y., Zhao, H., Zheng, Y., Geng, G., Li, M., Liu, F., Zhang, Y., Zheng, B., Clarke, L., and Zhang, Q.: Dynamic projection of anthropogenic emissions in China: methodology and 2015–2050 emission pathways under a range of socio-economic, climate policy, and pollution control scenarios, Atmos. Chem. Phys., 20, 5729–5757, https://doi.org/10.5194/acp-20-5729-2020, 2020.

https://doi.org/10.5194/egusphere-2026-3527
Preprint. Discussion started: 9 July 2026

Wunch, D., Wennberg, P. O., Osterman, G., Fisher, B., Naylor, B., Roehl, C. M., O'Dell, C., Mandrake, L., Viatte, C., Kiel, M., Griffith, D. W. T., Deutscher, N. M., Velazco, V. A., Notholt, J., Warneke, T., Petri, C., De Maziere, M., Sha, M. K., Sussmann, R., Rettinger, M., Pollard, D., Robinson, J., Morino, I., Uchino, O., Hase, F., Blumenstock, T., Feist, D. G., Arnold, S. G., Strong, K., Mendonca, J., Kivi, R., Heikkinen, P., Iraci, L., Podolske, J., Hillyard, P. W., Kawakami, S., Dubey, M. K., Parker, H. A., Sepulveda, E., García, O. E., Te, Y., Jeseck, P., Gunson, M. R., Crisp, D., and Eldering, A.: Comparisons of the Orbiting Carbon Observatory-2 (OCO-2) XCO2 measurements with TCCON, Atmos. Meas. Tech., 10, 2209–2238, https://doi.org/10.5194/amt-10-2209-2017, 2017.

Xu, R., Tong, D., Xiao, Q., Qin, X., Chen, C., Yan, L., Cheng, J., Cui, C., Hu, H., Liu, W., Yan, X., Wang, H., Liu, X., Geng, G., Lei, Y., Guan, D., He, K., and Zhang, Q.: MEIC-global-CO2: A new global CO2 emission inventory with highly resolved source category and sub-country information, Sci. China Earth Sci., 66, 2740–2756, https://doi.org/10.1007/s11430-023-1230-3, 2023.

Zeng, Y. and Hopke, P. K.: A study of the sources of acid precipitation in Ontario, Canada, Atmos. Environ., 23, 1499–1509, https://doi.org/10.1016/0004-6981(89)90409-5, 1989.

Zhang, L., Ruan, J., Zhang, Z., Qin, Z., Lei, Z., Cai, B., Wang, S., and Tang, L.: City-level pathways to carbon peak and neutrality in China, Cell Rep. Sustain., 1, 100102, https://doi.org/10.1016/j.crsus.2024.100102, 2024.

Zhang, S. and Chen, W.: Assessing the energy transition in China towards carbon neutrality with a probabilistic framework, Nat. Commun., 13, 87, https://doi.org/10.1038/s41467-021-27671-0, 2022a.

Zhang, S. and Chen, W.: China's energy transition pathway in a carbon neutral vision, Engineering, 14, 64–76, https://doi.org/10.1016/j.eng.2021.09.004, 2022b.

Zheng, B., Chevallier, F., Ciais, P., Broquet, G., Wang, Y., Lian, J., and Zhao, Y.: Observing carbon dioxide emissions over China's cities and industrial areas with the Orbiting Carbon Observatory-2, Atmos. Chem. Phys., 20, 8501–8510, https://doi.org/10.5194/acp-20-8501-2020, 2020.

Zhong, J., Zhang, X., Zhang, D., Wang, D., Guo, L., Peng, H., and Lu, Y.: Plausible global emissions scenario for 2 °C aligned with China's net-zero pathway, Nat. Commun., 16, 8102, https://doi.org/10.1038/s41467-025-62983-5, 2025.

Zhou, X., Liang, Y., Li, L., Chai, D., Gu, X., Yang, L., and Duan, J.: Analysis of spatial and temporal characteristics and influence mechanisms of carbon emissions in China, 1997–2017, J. Clean. Prod., 485, 144411, https://doi.org/10.1016/j.jclepro.2024.144411, 2024.